A three-dimensional layer-wise formulation for the coupled thermo-magneto-elastic analysis of multilayered composite flat and curved panels

Journal of
Composites Science

MDPI

Article

A Three-Dimensional Layer-Wise Formulation for the Coupled Thermo-Magneto-Elastic Analysis of Multilayered Composite Flat and Curved Panels

Salvatore Brischetto * and **Domenico Cesare**

Department of Mechanical and Aerospace Engineering, Politecnico di Torino, Corso Duca degli Abruzzi 24, 10129 Torino, Italy; domenico.cesare@polito.it
* Correspondence: salvatore.brischetto@polito.it; Tel.: +39-011-090-6813

Abstract

A fully coupled three-dimensional (3D) thermo-magneto-elastic layer-wise formulation is developed for the analysis of multilayered flat and curved panels used in aerospace and aeronautical applications. The model relies on a system of coupled second-order differential equations along the thickness coordinate z, formulated in a mixed orthogonal curvilinear reference system. The governing equations combine the three-dimensional equilibrium equations with the magnetic induction divergence equation and the heat conduction equation, providing a unified multifield framework for thermo-magneto-elastic analyses. Through a suitable definition of the curvature parameters, the same formulation can be directly applied to plates, cylinders, cylindrical panels, and shells with constant radii of curvature. The governing equations are analytically solved by adopting harmonic expansions in the in-plane directions together with the exponential matrix method along the thickness coordinate. The harmonic representation naturally satisfies simply-supported boundary conditions along the panel edges. The multilayered structure is modeled according to a layer-wise strategy, where the continuity of the selected mechanical, magnetic, and thermal variables is enforced across the interfaces between adjacent layers. Different loading boundary conditions can be assigned at the external surfaces by prescribing pressure loads, magnetic potential, transverse magnetic induction, and over-temperature. The numerical investigation is divided into two stages. First, the accuracy of the proposed formulation is verified through comparisons with thermo-magneto-elastic solutions available in the literature. Then, a comprehensive set of new benchmark results is presented by considering different geometries, thickness ratios, and loading boundary conditions. Both tabulated values and through-the-thickness distributions are reported for the most significant field variables. These benchmark results provide useful reference data for the assessment and validation of future two-dimensional and three-dimensional analytical and numerical formulations devoted to coupled thermo-magneto-elastic problems.

Keywords: three-dimensional formulation; thermo-magneto-elastic analysis; multilayered shell structures; layer-wise modeling; exponential matrix method; coupled multifield analysis

Check for updates

Academic Editor: Haifeng Zhao

Received: 1 July 2026
Revised: 2 August 2026
Accepted: 3 August 2026
Published: 5 August 2026

1. Introduction

Aerospace structures operate under service conditions where several physical fields interact simultaneously. The mutual interaction among these fields may significantly influence the structural response and generate deformation mechanisms that cannot be captured through uncoupled analyses [1,2]. Among the various multifield phenomena, thermo-magneto-elastic coupling represents a particularly relevant topic for advanced aerospace applications, including spacecraft, satellites, and launch vehicles. Although the scientific and industrial interest in this research area has steadily increased in recent years, only a limited number of contributions have addressed the fully coupled thermo-magneto-elastic problem. Experimental investigations are also of considerable importance, since they provide a deeper understanding of the interactions among the thermal, magnetic, and elastic fields under prescribed loading conditions. Such analyses make it possible to distinguish the contribution of each physical field to the overall coupled response. A practical application is the production of piezomagnetic actuators on the wing surface used to control the aero-elastic response in terms of flutter, vibrations and deformations. During operative flight conditions, possible increase in temperature on these piezomagnetic actuators can occur. In addition, the direct piezomagnetic effect offers the possibility of designing actuators capable of producing strains and displacements under externally applied magnetic fields, whereas the inverse piezomagnetic effect provides the basis for sensing devices able to detect deformations and displacements generated by combined thermal and mechanical actions.

Thermo-magneto-elastic coupling has been investigated in the literature for both flat and curved structural configurations. Concerning flat structures, including beams and plates, several contributions have been reported. For what concerns one-dimensional models, Guo and Alam [3] investigated the nonlinear bending response and thermal post-buckling behaviour of magneto-electro-elastic (MEE) beams by incorporating surface molecular effects within a nonlocal strain–gradient continuum framework. A node-based smoothed radial point interpolation formulation was proposed by Ren et al. [4] to investigate the free vibration characteristics and thermo-mechanical behaviour of functionally graded MEE structures. The same research group subsequently extended the formulation to the transient thermo-mechanical analysis of functionally graded MEE components containing cut-outs and operating under thermal loading conditions [5]. The influence of size-dependent effects on the buckling and free-vibration responses of functionally graded magneto-electro-thermo-elastic Timoshenko nanobeams was later examined by Ren and Qing [6]. A fully three-dimensional finite element formulation for multilayered MEE beams subjected to thermal loading was introduced by Vinyas and Kattimani [7]. Zhang et al. [8] employed a higher-order shear deformation beam model combined with von Kármán geometric nonlinearity to investigate the nonlinear bending and vibration behaviour of laminated MEE beams under thermal environments. In a subsequent study, the same authors [9] adopted the generalized differential quadrature method together with the Timoshenko beam theory and von Kármán nonlinear kinematics to analyse the thermal post-buckling response of laminated MEE beams. In the framework of bi-dimensional models including plates, Thuy Anh et al. [10] investigated the nonlocal static behaviour of magneto-electro-elastic sandwich micro- and nano-plates reinforced with functionally graded carbon nanotubes and operating under hygrothermal conditions. Esen and Ozmen [11] analysed the thermal vibration and buckling behaviour of porous nanoplates made of functionally graded barium titanate and cobalt ferrite materials. The coupled thermo-magneto-electro-elastic response of heterogeneous circular plates subjected to uniformly distributed thermal loads along the boundary was examined by Li et al. [12]. In a subsequent contribution, the same authors [13] developed a coupled cell-based smoothed finite element formulation to study the dynamic behaviour of functionally graded MEE thin-walled structures subjected to combined mechanical loading and thermal environments. Mahesh [14,15] proposed a finite element framework integrated with an artificial neural network algorithm to predict both the static response and the nonlinear pyro-coupled deflection of smart sandwich plates composed of a porous agglomerated carbon nanotube nanocomposite core and piezo-magneto-thermo-electric face sheets. Mohammadimehr et al. [16] carried out bending, buckling, and free-vibration analyses of microcomposite circular-annular sandwich plates subjected to hydro-thermo-magneto-mechanical loading conditions. AlMukahal et al. [17] proposed a numerical procedure for the axisymmetric bending analysis of functionally graded graphene platelet-reinforced annular sandwich nanoplates with porous cores. Talleb and Ren [18] introduced a multiscale analytical magneto-elastic formulation to characterize magnetostrictive structures under coupled magnetic, thermal, and mechanical loadings. Vinyas and Kattimani [19,20] presented a three-dimensional finite element formulation to investigate both the thermo-multiphysics response of multilayered MEE plates and the static behaviour of MEE plates subjected to hygrothermal loading conditions. Vu and Tran [21] investigated the thermo-electro-magneto-mechanical free-vibration response of sandwich plates with a graphene oxide powder-reinforced nanocomposite core and functionally graded MEE outer layers. Wang et al. [22] analysed the coupled magneto-thermo-elastic behaviour of simply supported soft ferromagnetic plates subjected to magnetic and thermal loading by adopting the linearized theory of magneto-elasticity together with a perturbation approach. Wu and Hsu [23] formulated a unified size-dependent shear deformation theory to investigate the free-vibration characteristics of functionally graded magneto-electro-elastic microplates under simply supported boundary conditions. Xing and Liu [24] employed the differential quadrature method to perform dynamic and quasi-static analyses of rectangular magneto-thermo-elastic plates under arbitrarily varying magnetic fields. Zhou et al. [25] proposed an inhomogeneous magneto-electro-elastic coupling element-free Galerkin formulation for static analyses. Saadatfar et al. [26] investigated the creep response of variable-thickness annular functionally graded MEE plates. Zenkour [27] examined the magneto-thermo-elastic behaviour of a functionally graded annular sandwich disk placed in a magnetic field and subjected to non-uniform steady-state thermal loading. More recently, Brischetto et al. [28,29] introduced a three-dimensional analytical coupled formulation for the static and free-vibration analysis of magneto-electro-elastic plates, where thermal effects and shell curvature were intentionally neglected.

The number of studies devoted to thermo-magneto-elastic coupling in curved structures, particularly shell configurations, is significantly smaller than that available for beams and plates. Among mono-dimensional and bi-dimensional curved models including both beams and plates, Pham et al. [30] analysed the free-vibration behaviour of a functionally graded porous curved nanobeam resting on an elastic foundation and operating under coupled hygro-thermo-magnetic conditions. An analytical formulation for anisotropic multilayer magneto-piezo-elastic hollow spheres and heterogeneous piezo-magneto-elastic discs subjected to coupled magneto-electro-hygro-thermo-mechanical loading was presented by Barati and Shariyat [31,32]. Bian and Tian [33] examined the thermo-magneto-elastic response of thin conductive spherical segment shells subjected to externally applied magnetic fields. Dai and Wang [34] derived an analytical solution describing the magneto-thermo-electro-elastic behaviour of a piezoelectric hollow cylinder immersed in an axial magnetic field and subjected to arbitrary thermal shocks, transient electrical excitations, and mechanical loading. Gui and Wu [35] analysed the buckling behaviour of thermo-magneto-electro-elastic nanocylindrical shells embedded in an elastic medium. Higuchi et al. [36,37] investigated the dynamic and quasi-static magneto-thermo-elastic stress fields generated by transient magnetic excitations in both solid and hollow conducting circular cylinders. Hu et al. [38,39] studied the coupled magneto-thermo-elastic vibration response of rotating and stationary ferromagnetic functionally graded cylindrical shells. Kong et al. [40] proposed an analytical framework for evaluating thermo-magneto-elastic stresses together with the perturbation of the magnetic field vector in non-homogeneous hollow cylinders subjected to thermal shock loading. The magneto-thermo-elastic behaviour of a thick double-walled cylinder composed of a functionally graded interlayer and a homogeneous outer layer was investigated by Loghman and Parsa [41]. Ni et al. [42] established a buckling formulation for magneto-electro-elastic composite cylindrical shells subjected to coupled hygro-thermo-magneto-electro-elastic loading conditions. Oveissi et al. [43] investigated hydro-magneto-electro wave propagation in an axially moving circular cylindrical nanoshell resting on an electromagnetic-visco-Pasternak foundation and conveying a magnetic nanofluid under different thermal and hygrothermal loading conditions. Selvamani et al. [44] adopted a multiple-scale perturbation technique to investigate the nonlinear wave propagation characteristics of doubly curved sandwich composite piezoelectric shells with flexible cores operating in hygrothermal environments. Tong et al. [45] introduced a three-phase cylindrical model for the analysis of fiber-reinforced composite structures subjected to in-plane mechanical loading under coupled thermal, electric, magnetic, and elastic fields. Tornabene et al. [46–48] proposed refined two-dimensional multifield formulations based on a generalized equivalent-layer-wise approach for the hygro-thermo-magneto-electro-elastic analysis of curved shell structures. Finally, Lang and Xuewu [49] presented a formulation capable of predicting both the buckling and free-vibration responses of functionally graded magneto-electro-thermo-elastic circular cylindrical shells. For what concerns three-dimensional model for curved thermo-magneto-elastic structures, a series of three-dimensional analytical formulations for the static and free-vibration analysis of spherical shells was proposed by Brischetto et al. [50–53], addressing thermo-elastic, magneto-elastic, and magneto-electro-elastic coupling phenomena. However, none of these contributions considered the fully coupled thermo-magneto-elastic problem. In addition, Ponnusamy and Selvamani [54] analysed the three-dimensional propagation of elastic waves in a homogeneous transversely isotropic magneto-thermo-elastic cylindrical panel.

The present manuscript introduces a fully coupled thermo-magneto-elastic formulation by simultaneously considering the thermal, magnetic, and elastic fields. In the previous works by the same authors, these three different fields were investigated separately or through different coupling configurations. The work [50] proposes the static and free vibration analysis of multilayered and functionally graded magneto-elastic structures. In ref. [51] is proposed the thermo-elastic behaviour of multilayered flat and curved structures. The works [52,53] coupled the electric, the magnetic and the elastic fields to evaluate the static and free vibration behaviour of curved smart structures. The main novelty of the present manuscript is the development of a fully coupled three-dimensional thermo-magneto-elastic model for the static analysis of flat and curved multilayered structures solved through the proposed mixed closed-form formulation.

The objective of the present work is the development of a three-dimensional thermo-magneto-elastic shell formulation suitable for both flat and curved multilayered panels. Curved geometries are described by adopting a mixed orthogonal curvilinear reference system (α, β, z), which provides a unified mathematical framework for the analysis of plates, cylinders, cylindrical panels, and spherical shells through the appropriate definition of the constant curvature radii R_α and R_β. One of the main features of the proposed formulation is therefore its ability to analyse different structural configurations within a unique thermo-magneto-elastic framework. The present model can analyse only cross-ply laminations by considering simply-supported edges. The model is governed by five coupled second-order differential equations expressed in terms of the displacement components, magnetic potential, and over-temperature. These equations are obtained by combining the three-dimensional elastic equilibrium equations with the magnetic induction divergence equation and the three-dimensional Fourier heat conduction equation. The resulting system is solved analytically by adopting Navier harmonic expansions in the in-plane directions together with the exponential matrix method along the thickness coordinate. Such a solution procedure enables an exact three-dimensional evaluation of the secondary field variables, including strains, stresses, magnetic induction components, and heat fluxes throughout the thickness. Finally, the multilayered configuration is represented through a layer-wise description in which interlaminar continuity conditions are enforced at every interface between adjacent layers.

The manuscript is organized as follows. Section 2 describes the theoretical framework of the proposed formulation, including the analytical derivation of the three-dimensional multifield governing, constitutive, and geometrical equations. Section 3 first presents a preliminary assessment to validate the proposed 3D thermo-magneto-elastic model for both flat and curved structures. It then introduces a set of new benchmark cases covering different thickness ratios, for which both tabulated results at selected through-the-thickness positions and graphical distributions of the main field variables are reported. These benchmarks illustrate the capability of the formulation to capture the effects associated with thermo-magneto-elastic coupling, material lay-up, thickness ratio, zigzag behaviour, and shell curvature. Finally, the main conclusions and the principal outcomes of the present study are summarized in Section 4.

2. 3D Thermo-Magneto-Elastic Static Analysis of Shells

This section presents the theoretical formulation adopted for the three-dimensional thermo-magneto-elastic static analysis of multilayered shell structures. The presentation is divided into four subsections. The first one introduces the three-dimensional multifield governing equations expressed in the mixed orthogonal curvilinear reference system. The constitutive relations and the multifield congruence equations are subsequently presented in the second and third subsections, respectively. The final subsection describes the analytical solution procedure based on the exponential matrix method.

2.1. 3D Multifield Governing Equations

The thermo-magneto-elastic static problem is governed by a system of five fully coupled three-dimensional equations. These consist of the three equilibrium equations for the elastic field, the divergence equation for the magnetic induction field, and the steady-state Fourier heat conduction equation. The steady-state condition implies the end of any transitory condition. The steady-state condition is the most onerous from a structural point of view. The complete system is formulated in the mixed orthogonal curvilinear reference system (α, β, z) illustrated in Figure 1. This coordinate system combines two curvilinear in-plane coordinates (α and β) with a rectilinear thickness coordinate (z), thus providing a unified framework for the analysis of different structural configurations. By assigning the appropriate values to the constant curvature radii R_α and R_β, the same formulation can be directly applied to plates, cylinders, cylindrical panels, and spherical shells.

The thermo-magneto-elastic governing equations for spherical shells are explicitly expressed as

$$H_\beta \sigma^k_{\alpha\alpha,\alpha} + H_\alpha \sigma^k_{\alpha\beta,\beta} + H_\alpha H_\beta \sigma^k_{\alpha z,z} + \left(\frac{2H_\beta}{R_\alpha} + \frac{H_\alpha}{R_\beta}\right)\sigma^k_{\alpha z} = 0, \quad (1)$$

$$H_\beta \sigma^k_{\alpha\beta,_\alpha} + H_\alpha \sigma^k_{\beta\beta,_\beta} + H_\alpha H_\beta \sigma^k_{\beta z,_z} + \left(\frac{2H_\alpha}{R_\beta} + \frac{H_\beta}{R_\alpha}\right)\sigma^k_{\beta z} = 0, \tag{2}$$

$$H_\beta \sigma^k_{\alpha z,_\alpha} + H_\alpha \sigma^k_{\beta z,_\beta} + H_\alpha H_\beta \sigma^k_{zz,_z} + \frac{H_\beta}{R_\alpha}\sigma^k_{\alpha\alpha} + \frac{H_\alpha}{R_\beta}\sigma^k_{\beta\beta} + \left(\frac{H_\beta}{R_\alpha} + \frac{H_\alpha}{R_\beta}\right)\sigma^k_{zz} = 0, \tag{3}$$

$$\frac{\mathcal{B}^k_{\alpha,_\alpha}}{H_\alpha} + \frac{\mathcal{B}^k_{\beta,_\beta}}{H_\beta} + \mathcal{B}^k_{z,_z} = 0, \tag{4}$$

$$\frac{q^k_{\alpha,_\alpha}}{H_\alpha} + \frac{q^k_{\beta,_\beta}}{H_\beta} + q^k_{z,_z} = 0. \tag{5}$$

where $\sigma^k_{\alpha\alpha}$, $\sigma^k_{\alpha\beta}$, $\sigma^k_{\alpha z}$, $\sigma^k_{\beta\beta}$, $\sigma^k_{\beta z}$, and σ^k_{zz} denote the six stress components, whereas $\mathcal{B}^k_\alpha$, $\mathcal{B}^k_\beta$, and $\mathcal{B}^k_z$ represent the magnetic induction components. Similarly, q^k_α, q^k_β, and q^k_z are the heat flux components. The subscripts $,\alpha$, $,\beta$, and $,z$ indicate partial differentiation with respect to the corresponding coordinates, while the superscript k identifies the physical layer. The quantities R_α and R_β denote the constant radii of curvature in the two in-plane directions. The formulation reported in Equations (1)–(5) follows the theoretical developments presented in [50,55,56]. The curvature parameters appearing in the governing equations are defined as

$$\begin{Bmatrix} H_\alpha \\ H_\beta \\ H_z \end{Bmatrix} = \begin{Bmatrix} H_\alpha(z) \\ H_\beta(z) \\ H_z(z) \end{Bmatrix} = \begin{Bmatrix} 1 + \dfrac{z}{R_\alpha} \\ 1 + \dfrac{z}{R_\beta} \\ 1 \end{Bmatrix} = \begin{Bmatrix} 1 + \dfrac{\tilde{z} - h/2}{R_\alpha} \\ 1 + \dfrac{\tilde{z} - h/2}{R_\beta} \\ 1 \end{Bmatrix}, \qquad -h/2 < z < h/2 \quad \text{or} \quad 0 < \tilde{z} < h. \tag{6}$$

h denotes the total thickness of the structure. The curvature coefficients H_α and H_β differ from unity because the α and β coordinates follow curved directions, whereas H_z is equal to one since the thickness coordinate z is rectilinear. For the sake of conciseness, the dependence of the curvature coefficients H_α and H_β on the thickness coordinate is omitted in the remainder of the paper, although it is implicitly retained throughout the formulation.

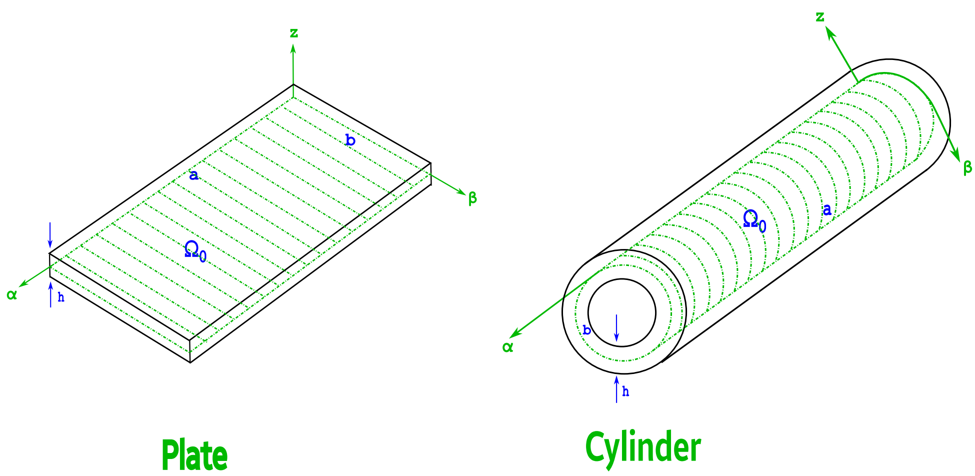

Figure 1. *Cont.*

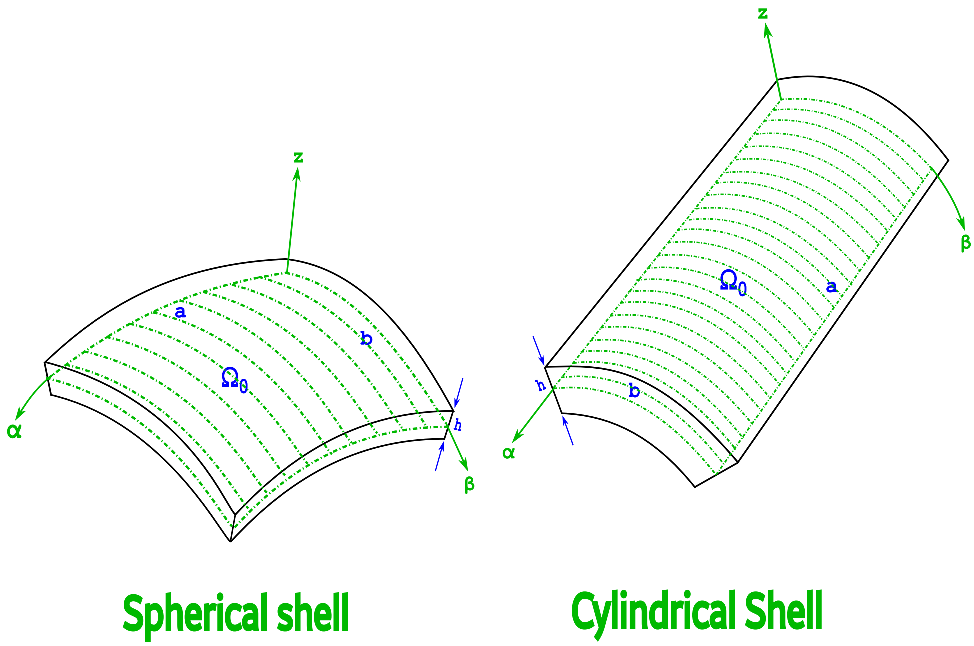

Figure 1. Geometries, mixed curvilinear orthogonal reference system and middle reference surface for Preliminary Assessments (PA) and New Cases (NC). Dotted lines represent the middle reference surface Ω_0. The mixed curvilinear orthogonal reference system is visible for each structure.

2.2. 3D Multifield Constitutive Equations

The constitutive relations governing the coupled thermo-magneto-elastic problem are derived from the definition of a multifield free energy density function. This function is expressed as

$$\mathcal{W}(\varepsilon_{ij}, \mathcal{H}_i, T, \theta)$$

where ε_{ij} denotes the strain tensor components, $\mathcal{H}_i$ represents the magnetic field components, T is the absolute temperature, and θ is the over-temperature, defined as $\theta = T - T_0$, with T_0 being the reference environmental temperature expressed in Kelvin. The adopted free energy density accounts for the elastic, magnetic, and thermal contributions together with all the associated coupling effects, namely the magneto-elastic, thermo-elastic, and thermo-magnetic interactions. Neglecting the entropy contribution, the free energy density assumes the following quadratic form:

$$\mathcal{W}(\varepsilon_{ij}, \mathcal{H}_i, \theta) = \frac{1}{2}\varepsilon_{ij} C_{ijkl} \varepsilon_{kl} - \varepsilon_{ij} r_{ijk} \mathcal{H}_k - \varepsilon_{ij} \lambda_{ij} \theta + \frac{1}{2} H_i \delta_{ij} H_j + H_i g_i \theta + \frac{1}{2}\theta^T k_{ij} \theta. \quad (7)$$

Here, C_{ijkl} denotes the elastic stiffness coefficients, r_{ijk} the piezomagnetic coefficients, λ_{ij} the thermo-elastic coefficients, δ_{ij} the magnetic permeability coefficients, g_i the thermo-magnetic coupling coefficients, and k_{ij} the thermal conductivity coefficients. The constitutive equations are then obtained by differentiating the free energy density with respect to the corresponding field variables:

$$\boldsymbol{\sigma} = \frac{\partial \mathcal{W}}{\partial \boldsymbol{\varepsilon}}, \quad (8)$$

$$\boldsymbol{\mathcal{B}} = \frac{\partial \mathcal{W}}{\partial \boldsymbol{H}}, \quad (9)$$

$$\boldsymbol{q} = -\frac{\partial \mathcal{W}}{\partial \theta}. \quad (10)$$

By evaluating Equations (8)–(10), the explicit form of the 3D thermo-magneto-elastic linear constant constitutive equations for orthotropic materials is obtained:

$$\sigma_{\alpha\alpha}^k = C_{11}^k \varepsilon_{\alpha\alpha}^k + C_{12}^k \varepsilon_{\beta\beta}^k + C_{13}^k \varepsilon_{zz}^k - r_{31}^k \mathcal{H}_z^k - \lambda_{11}^k \theta^k, \tag{11}$$

$$\sigma_{\beta\beta}^k = C_{12}^k \varepsilon_{\alpha\alpha}^k + C_{22}^k \varepsilon_{\beta\beta}^k + C_{23}^k \varepsilon_{zz}^k - r_{32}^k \mathcal{H}_z^k - \lambda_{22}^k \theta^k, \tag{12}$$

$$\sigma_{zz}^k = C_{13}^k \varepsilon_{\alpha\alpha}^k + C_{23}^k \varepsilon_{\beta\beta}^k + C_{33}^k \varepsilon_{zz}^k - r_{33}^k \mathcal{H}_z^k - \lambda_{33}^k \theta^k, \tag{13}$$

$$\sigma_{\beta z}^k = C_{44}^k \gamma_{\beta z}^k - r_{24}^k \mathcal{H}_\beta^k, \tag{14}$$

$$\sigma_{\alpha z}^k = C_{55}^k \gamma_{\alpha z}^k - r_{15}^k \mathcal{H}_\alpha^k, \tag{15}$$

$$\sigma_{\alpha\beta}^k = C_{66}^k \gamma_{\alpha\beta}^k, \tag{16}$$

$$\mathcal{B}_\alpha^k = r_{15}^k \gamma_{\alpha z}^k + \delta_{11}^k \mathcal{H}_\alpha^k, \tag{17}$$

$$\mathcal{B}_\beta^k = r_{24}^k \gamma_{\beta z}^k + \delta_{22}^k \mathcal{H}_\beta^k, \tag{18}$$

$$\mathcal{B}_z^k = r_{31}^k \varepsilon_{\alpha\alpha}^k + r_{32}^k \varepsilon_{\beta\beta}^k + r_{33}^k \varepsilon_{zz}^k + \delta_{33}^k \mathcal{H}_z^k + g_3^k \theta^k, \tag{19}$$

$$q_\alpha^k = -\frac{k_{11}^k}{H_\alpha} \theta_{,\alpha}^k, \tag{20}$$

$$q_\beta^k = -\frac{k_{22}^k}{H_\beta} \theta_{,\beta}^k, \tag{21}$$

$$q_z^k = -k_{33}^k \theta_{,z}^k, \tag{22}$$

where $\varepsilon_{\alpha\alpha}^k$, $\varepsilon_{\beta\beta}^k$, ε_{zz}^k, $\gamma_{\beta z}^k$, $\gamma_{\alpha z}^k$, and $\gamma_{\alpha\beta}^k$ denote the six strain components. The elastic behaviour of the cross-ply orthotropic lamina is described by the stiffness coefficients C_{11}^k, C_{12}^k, C_{13}^k, C_{22}^k, C_{23}^k, C_{33}^k, C_{44}^k, C_{55}^k, and C_{66}^k. The piezomagnetic coupling is characterized by the coefficients r_{31}^k, r_{32}^k, r_{33}^k, r_{24}^k, and r_{15}^k, while $\mathcal{H}_\alpha^k$, $\mathcal{H}_\beta^k$, and $\mathcal{H}_z^k$ represent the magnetic field components. The thermo-elastic coupling coefficients are denoted by λ_{11}^k, λ_{22}^k, and λ_{33}^k. The over-temperature is indicated by θ^k, with $\theta = T - T_0$ and T_0 representing the reference environmental temperature expressed in Kelvin. The magnetic permeability coefficients are given by δ_{11}^k, δ_{22}^k, and δ_{33}^k, whereas g_3^k is the thermo-magnetic coupling coefficient relating the over-temperature to the transverse magnetic induction component. Finally, k_{11}^k, k_{22}^k, and k_{33}^k are the thermal conductivity coefficients.

The constitutive relations reported in Equations (11)–(22) provide a fully coupled description of the mechanical, magnetic, and thermal behaviour of the multilayered material.

2.3. 3D Multifield Congruence Equations

The 3D multifield linear congruence equations establish the kinematic relationships for small deformations of the thermo-magneto-elastic problem by linking the displacement field with the strain components and the magnetic potential with the magnetic field. Their explicit form is given by

$$\varepsilon_{\alpha\alpha}^k = \frac{u_{,\alpha}^k}{H_\alpha} + \frac{w^k}{H_\alpha R_\alpha}, \tag{23}$$

$$\varepsilon_{\beta\beta}^k = \frac{v_{,\beta}^k}{H_\beta} + \frac{w^k}{H_\beta R_\beta}, \tag{24}$$

$$\varepsilon_{zz}^k = w_{,z}^k, \tag{25}$$

$$\gamma^k_{\alpha\beta} = \frac{v^k_{,\alpha}}{H_\alpha} + \frac{u^k_{,\beta}}{H_\beta}, \tag{26}$$

$$\gamma^k_{\alpha z} = \frac{w^k_{,\alpha}}{H_\alpha} + u^k_{,z} - \frac{u^k}{H_\alpha R_\alpha}, \tag{27}$$

$$\gamma^k_{\beta z} = \frac{w^k_{,\beta}}{H_\beta} + v^k_{,z} - \frac{v^k}{H_\beta R_\beta}. \tag{28}$$

$$\mathcal{H}^k_\alpha = -\frac{\psi^k_{,\alpha}}{H_\alpha}, \tag{29}$$

$$\mathcal{H}^k_\beta = -\frac{\psi^k_{,\beta}}{H_\beta}, \tag{30}$$

$$\mathcal{H}^k_z = -\psi^k_{,z}. \tag{31}$$

Here, ψ^k denotes the magnetic potential associated with the k-th physical layer. Together, Equations (23)–(31) provide the kinematic description required to couple the mechanical and magnetic fields within the proposed three-dimensional formulation.

2.4. Analytical Solution via the Exponential Matrix Method

This subsection presents the analytical solution procedure via the exponential matrix method. By recursively introducing the 3D multifield congruence equations in Equations (23)–(31) into the constitutive equations in Equations (11)–(22), and subsequently substituting the resulting expressions into the governing equations in Equations (1)–(5), the complete system can be reformulated in terms of the primary variables u, v, w, ψ, and θ. These variables represent the three displacement components, the magnetic potential, and the over-temperature, respectively, and constitute the primary unknowns of the coupled thermo-magneto-elastic problem.

The analytical solution is obtained by expressing the primary variables through Navier harmonic expansions. Their explicit expressions are given by

$$u^k(\alpha,\beta,z) = U^k(z)\cos(\bar{\alpha}\alpha)\sin(\bar{\beta}\beta), \tag{32}$$

$$v^k(\alpha,\beta,z) = V^k(z)\sin(\bar{\alpha}\alpha)\cos(\bar{\beta}\beta), \tag{33}$$

$$w^k(\alpha,\beta,z) = W^k(z)\sin(\bar{\alpha}\alpha)\sin(\bar{\beta}\beta), \tag{34}$$

$$\psi^k(\alpha,\beta,z) = \Psi^k(z)\sin(\bar{\alpha}\alpha)\sin(\bar{\beta}\beta), \tag{35}$$

$$\theta^k(\alpha,\beta,z) = \Theta^k(z)\sin(\bar{\alpha}\alpha)\sin(\bar{\beta}\beta). \tag{36}$$

The functions $U^k(z)$, $V^k(z)$, $W^k(z)$, $\Psi^k(z)$, and $\Theta^k(z)$ represent the through-the-thickness amplitudes of the corresponding field variables and constitute the unknown functions of the coupled thermo-magneto-elastic problem. The harmonic coefficients are defined in terms of the half-wave numbers m and n and the panel dimensions a and b as

$$\bar{\alpha} = \frac{m\pi}{a}, \qquad \bar{\beta} = \frac{n\pi}{b}.$$

Imposition of Navier harmonic forms permits the satisfaction of simply-supported boundary conditions and the exact computation of the derivatives along α and β directions. In this way, the 3D governing equations for the 3D thermo-magneto-elastic problem can be written in explicit form as:

$$
\begin{aligned}
&\left(-\frac{H_\beta C_{55}^k}{H_\alpha R_\alpha^2}-\frac{C_{55}^k}{R_\alpha R_\beta}-\bar{\alpha}^2\frac{C_{11}^k H_\beta}{H_\alpha}-\bar{\beta}^2\frac{C_{66}^k H_\alpha}{H_\beta}\right)U^k+\left(-\bar{\alpha}\bar{\beta}C_{12}^k-\bar{\alpha}\bar{\beta}C_{66}^k\right)V^k+\\
&+\left(\bar{\alpha}\frac{C_{11}^k H_\beta}{H_\alpha R_\alpha}+\bar{\alpha}\frac{C_{12}^k}{R_\beta}+\bar{\alpha}\frac{C_{55}^k H_\beta}{H_\alpha R_\alpha}+\bar{\alpha}\frac{C_{55}^k}{R_\beta}\right)W^k+\left(\frac{C_{55}^k H_\beta}{R_\alpha}+\frac{C_{55}^k H_\alpha}{R_\beta}\right)U_{,z}^k+\\
&+\left(\bar{\alpha}C_{13}^k H_\beta+\bar{\alpha}C_{55}^k H_\beta\right)W_{,z}^k+\left(C_{55}^k H_\alpha H_\beta\right)U_{,zz}^k+\left(+2\bar{\alpha}\frac{r_{15}^k H_\beta}{H_\alpha R_\alpha}+\bar{\alpha}\frac{r_{15}^k}{R_\beta}\right)\Psi^k+\\
&+\left(\bar{\alpha}r_{31}^k H_\beta+\bar{\alpha}r_{15}^k H_\beta\right)\Psi_{,z}^k-\left(\bar{\alpha}\lambda_{11}^k H_\beta\right)\Theta^k=0,
\end{aligned}
\tag{37}
$$

$$
\begin{aligned}
&\left(-\frac{H_\alpha C_{44}^k}{H_\beta R_\beta^2}-\frac{C_{44}^k}{R_\alpha R_\beta}-\bar{\alpha}^2\frac{C_{66}^k H_\beta}{H_\alpha}-\bar{\beta}^2\frac{C_{22}^k H_\alpha}{H_\beta}\right)V^k+\left(-\bar{\alpha}\bar{\beta}C_{12}^k-\bar{\alpha}\bar{\beta}C_{66}^k\right)U^k+\\
&+\left(\bar{\beta}\frac{C_{44}^k H_\alpha}{H_\beta R_\beta}+\bar{\beta}\frac{C_{44}^k}{R_\alpha}+\bar{\beta}\frac{C_{22}^k H_\alpha}{H_\beta R_\beta}+\bar{\beta}\frac{C_{12}^k}{R_\alpha}\right)W^k+\left(\frac{C_{44}^k H_\alpha}{R_\beta}+\frac{C_{44}^k H_\beta}{R_\alpha}\right)V_{,z}^k+\\
&+\left(\bar{\beta}C_{44}^k H_\alpha+\bar{\beta}C_{23}^k H_\alpha\right)W_{,z}^k+\left(C_{44}^k H_\alpha H_\beta\right)V_{,zz}^k+\left(+2\bar{\beta}\frac{r_{24}^k H_\alpha}{H_\beta R_\beta}+\bar{\beta}\frac{r_{24}^k}{R_\alpha}\right)\Psi^k+\\
&+\left(\bar{\beta}r_{32}^k H_\alpha+\bar{\beta}r_{24}^k H_\alpha\right)\Psi_{,z}^k-\left(\bar{\beta}\lambda_{22}^k H_\alpha\right)\Theta^k=0,
\end{aligned}
\tag{38}
$$

$$
\begin{aligned}
&\left(\frac{C_{13}^k}{R_\alpha R_\beta}+\frac{C_{23}^k}{R_\alpha R_\beta}-\frac{C_{11}^k H_\beta}{H_\alpha R_\alpha^2}-\frac{2C_{12}^k}{R_\alpha R_\beta}-\frac{C_{22}^k H_\alpha}{H_\beta R_\beta^2}-\bar{\alpha}^2\frac{C_{55}^k H_\beta}{H_\alpha}-\bar{\beta}^2\frac{C_{44}^k H_\alpha}{H_\beta}\right)W^k+\\
&+\left(\bar{\alpha}\frac{C_{55}^k H_\beta}{H_\alpha R_\alpha}-\bar{\alpha}\frac{C_{13}^k}{R_\beta}+\bar{\alpha}\frac{C_{11}^k H_\beta}{H_\alpha R_\alpha}+\bar{\alpha}\frac{C_{12}^k}{R_\beta}\right)U^k+\left(\bar{\beta}\frac{C_{44}^k H_\alpha}{H_\beta R_\beta}-\bar{\beta}\frac{C_{23}^k}{R_\alpha}+\bar{\beta}\frac{C_{22}^k H_\alpha}{H_\beta R_\beta}+\bar{\beta}\frac{C_{12}^k}{R_\alpha}\right)V^k+\\
&+\left(-\bar{\alpha}C_{55}^k H_\beta-\bar{\alpha}C_{13}^k H_\beta\right)U_{,z}^k+\left(-\bar{\beta}C_{44}^k H_\alpha-\bar{\beta}C_{23}^k H_\alpha\right)V_{,z}^k+\left(\frac{C_{33}^k H_\beta}{R_\alpha}+\frac{C_{33}^k H_\alpha}{R_\beta}\right)W_{,z}^k+\\
&+\left(-\bar{\alpha}^2\frac{r_{15}^k H_\beta}{H_\alpha}-\bar{\beta}^2\frac{r_{24}^k H_\alpha}{H_\beta}\right)\Psi^k+\left(-\frac{r_{31}^k H_\beta}{R_\alpha}-\frac{r_{32}^k H_\alpha}{R_\beta}+\frac{r_{33}^k H_\beta}{R_\alpha}+\frac{r_{33}^k H_\alpha}{R_\beta}\right)\Psi_{,z}^k+\\
&+\left(C_{33}^k H_\alpha H_\beta\right)W_{,zz}^k+\left(r_{33}^k H_\alpha H_\beta\right)\Psi_{,zz}^k+\left(\frac{\lambda_{11}^k H_\beta}{R_\alpha}+\frac{\lambda_{22}^k H_\alpha}{R_\beta}-\frac{\lambda_{33}^k H_\beta}{R_\alpha}-\frac{\lambda_{33}^k H_\alpha}{R_\beta}\right)\Theta^k+\\
&-\left(\lambda_{33}H_\alpha H_\beta\right)\Theta_{,z}^k=0,
\end{aligned}
\tag{39}
$$

$$
\begin{aligned}
&\left(\bar{\alpha}\frac{r_{15}^k}{H_\alpha^2 R_\alpha}\right)U^k+\left(\bar{\beta}\frac{r_{24}^k}{H_\beta^2 R_\beta}\right)V^k+\left(-\bar{\alpha}^2\frac{r_{15}^k}{H_\alpha^2}-\bar{\beta}^2\frac{r_{24}^k}{H_\beta^2}\right)W^k+\left(-\bar{\alpha}\frac{r_{15}^k}{H_\alpha}-\bar{\alpha}\frac{r_{31}^k}{H_\alpha}\right)U_{,z}^k+\\
&+\left(-\bar{\beta}\frac{r_{24}^k}{H_\beta}-\bar{\beta}\frac{r_{32}^k}{H_\beta}\right)V_{,z}^k+\left(\frac{r_{31}^k}{H_\alpha R_\alpha}+\frac{r_{32}^k}{H_\beta R_\beta}\right)W_{,z}^k+\left(r_{33}^k\right)W_{,zz}^k+\left(\bar{\alpha}^2\frac{\delta_{11}^k}{H_\alpha^2}+\bar{\beta}^2\frac{\delta_{22}^k}{H_\beta^2}\right)\Psi^k+\\
&-\left(\delta_{33}^k\right)\Psi_{,zz}^k+\\
&+\left(g_3^k\right)\Theta_{,z}^k=0,
\end{aligned}
\tag{40}
$$

$$
\left(-\bar{\alpha}^2\frac{k_{11}^k}{H_\alpha^2}-\bar{\beta}^2\frac{k_{22}^k}{H_\beta^2}\right)\Theta^k+\left(k_{33}^k\right)\Theta_{,zz}^k=0.
\tag{41}
$$

Subscripts $,z$ and $,zz$ indicate first and second derivatives in z, respectively. Equations (37)–(41) couple the thermal, the magnetic and the elastic physical fields thanks to the pyromagnetic coefficients, the piezomagnetic coefficients and the thermo-elastic coupling coefficients. For the sake of compactness, all the coefficient groups enclosed within parentheses in Equations (37)–(41) are replaced by the coefficients A_i^k and J_i^k. Accordingly, the governing system can be rewritten in the following compact form:

$$A_1^k U^k + A_2^k V^k + A_3^k W^k + A_4^k \Psi^k + J_1^k \Theta^k + A_5^k U_{,z}^k + A_6^k W_{,z}^k + A_7^k \Psi_{,z}^k + A_8^k U_{,zz}^k = 0, \tag{42}$$

$$A_9^k U^k + A_{10}^k V^k + A_{11}^k W^k + A_{12}^k \Psi^k + J_2^k \Theta^k + A_{13}^k V_{,z}^k + A_{14}^k W_{,z}^k + A_{15}^k \Psi_{,z}^k + A_{16}^k V_{,zz}^k = 0, \tag{43}$$

$$\begin{aligned} A_{17}^k U^k + A_{18}^k V^k + A_{19}^k W^k + A_{20}^k \Psi^k + J_3^k \Theta^k + A_{21}^k U_{,z}^k + A_{22}^k V_{,z}^k + A_{23}^k W_{,z}^k + A_{24}^k \Psi_{,z}^k + J_4^k \Theta_{,z}^k + \\ + A_{25}^k W_{,zz}^k + A_{26}^k \Psi_{,zz}^k = 0, \end{aligned} \tag{44}$$

$$\begin{aligned} A_{27}^k U^k + A_{28}^k V^k + A_{29}^k W^k + A_{30}^k \Psi^k + A_{31}^k U_{,z}^k + A_{32}^k V_{,z}^k + A_{33}^k W_{,z}^k + J_5^k \Theta_{,z}^k + \\ + A_{34}^k W_{,zz}^k + A_{35}^k \Psi_{,zz}^k = 0, \end{aligned} \tag{45}$$

$$J_6^k \Theta^k + J_7^k \Theta_{,zz}^k = 0. \tag{46}$$

Equations (42)–(46) form a coupled system of second-order ordinary differential equations along the thickness coordinate z. The exponential matrix method requires both constant coefficients and a first-order differential formulation. However, the coefficients A_i^k depend on the curvature functions H_α and H_β, which vary through the thickness. To overcome this issue, each physical layer is subdivided into a set of sufficiently thin mathematical layers in which the thickness coordinate can be assumed constant. Consequently, the curvature terms, together with the associated coefficients A_i^k and J_i^k, become constant within each mathematical layer.

Let M denote the total number of mathematical layers used to discretize the thickness, and let j identify a generic mathematical layer. Since the governing equations have the same form in every mathematical layer, the following derivation is presented for a generic layer j. The second-order system is subsequently transformed into an equivalent first-order one by introducing the first derivatives of the primary variables through a standard doubling procedure. The resulting equations are

$$A_8^j U_{,z}^j = A_8^j U_{,z}^j, \tag{47}$$

$$A_{16}^j V_{,z}^j = A_{16}^j V_{,z}^j, \tag{48}$$

$$P_1^j W_{,z}^j = P_1^j W_{,z}^j, \tag{49}$$

$$P_1^j \Psi_{,z}^j = P_1^j \Psi_{,z}^j, \tag{50}$$

$$J_7^j \Theta_{,z}^j = J_7^j \Theta_{,z}^j, \tag{51}$$

$$A_8^j U_{,zz}^j = -A_1^j U^j - A_2^j V^j - A_3^j W^j - A_4^j \Psi^j - J_1^k \Theta^k - A_5^j U_{,z}^j - A_6^j W_{,z}^j - A_7^j \Psi_{,z}^j, \tag{52}$$

$$A_{16}^j V_{,zz}^j = -A_9^j U^j - A_{10}^j V^j - A_{11}^j W^j - A_{12}^j \Psi^j - J_2^k \Theta^k - A_{13}^j V_{,z}^j - A_{14}^j W_{,z}^j - A_{15}^j \Psi_{,z}^j, \tag{53}$$

$$P_1^j W_{,zz}^j = -P_2^j U^j - P_3^j V^j - P_4^j W^j - P_5^j \Theta^j - P_6^j \Psi^j - P_7^j U_{,z}^j - P_8^j V_{,z}^j - P_9^j W_{,z}^j - P_{10}^j \Psi_{,z}^j - P_{11}^j \Theta_{,z}^j, \tag{54}$$

$$P_1^j \Psi_{,zz}^j = -P_{12}^j U^j - P_{13}^j V^j - P_{14}^j W^j - P_{15}^j \Psi^j - P_{16}^j U_{,z}^j - P_{17}^j V_{,z}^j - P_{18}^j W_{,z}^j - P_{19}^j \Theta_{,z}^j, \tag{55}$$

$$J_7^j \Theta_{,zz}^j = -J_6^j \Theta^j, \tag{56}$$

The above first-order representation is directly suitable for the application of the exponential matrix method. Accordingly, Equations (47)–(56) can be assembled into the following state-space form:

$$\boldsymbol{D}^j \boldsymbol{X}_{,z}^j = \boldsymbol{A}^j \boldsymbol{X}^j \qquad \Rightarrow \qquad \boldsymbol{X}_{,z}^j = \boldsymbol{A}^{*j} \boldsymbol{X}^j, \tag{57}$$

where $\boldsymbol{D}^j$ and $\boldsymbol{A}^j$ are two 10×10 coefficient matrices. $\boldsymbol{X}^j = \{U^j \; V^j \; W^j \; \Psi^j \; \Theta^j \; U^j_{,z} \; V^j_{,z} \; W^j_{,z} \; \Psi^j_{,z} \; \Theta^j_{,z}\}^T$ is the 10×1 state vector, and $\boldsymbol{X}^j_{,z}$ denotes its derivative with respect to the thickness coordinate. Owing to the doubling procedure, the first derivatives of the original unknowns are incorporated into the state vector, leading to a first-order system with ten independent variables. The first-order state-space system in Equation (57) admits an analytical solution based on the exponential matrix method. The solution relates the state vector at the bottom of the generic mathematical layer ($z = 0$) to that at its top ($z = h_j$), and can be written as

$$\boldsymbol{X}^j\left(h_j\right) = \boldsymbol{A}^{**j}\boldsymbol{X}^j(0), \qquad where \qquad \boldsymbol{A}^{**j} = \exp\left(\boldsymbol{A}^{*j}h_j\right) = \sum_{i=0}^{N} \frac{\left(\boldsymbol{A}^{*j}\right)^i h_j^i}{i!}. \tag{58}$$

The matrix $\boldsymbol{A}^{**j}$ is the 10×10 exponential matrix associated with the j-th mathematical layer, whereas h_j denotes its thickness. In the present formulation, the exponential matrix is evaluated through the truncated Taylor series expansion reported in Equation (58), where N is the order of the approximation. The first term of the series corresponds to the identity matrix, namely $\left(\boldsymbol{A}^{*j}\right)^0 = \boldsymbol{I}$, with $\boldsymbol{I}$ denoting the 10×10 identity matrix.

The layer-wise description of the multilayered structure is achieved by enforcing interlaminar continuity conditions at every interface between two adjacent mathematical layers. These interlaminar continuity conditions imply the perfect interface hypothesis. These continuity conditions involve both primary variables (displacements, magnetic potential, and over-temperature) and secondary variables (transverse shear and normal stresses, transverse magnetic induction, and transverse heat flux). Their enforcement guarantees the continuity of the thermo-magneto-elastic fields throughout the thickness direction. The interlaminar continuity conditions can be expressed as

$$u_b^j = u_t^{j-1}, \quad v_b^j = v_t^{j-1}, \quad w_b^j = w_t^{j-1}, \quad \psi_b^j = \psi_t^{j-1}, \quad \theta_b^j = \theta_t^{j-1}, \tag{59}$$

$$\sigma^j_{\alpha z_b} = \sigma^{j-1}_{\alpha z_t}, \quad \sigma^j_{\beta z_b} = \sigma^{j-1}_{\beta z_t}, \quad \sigma^j_{zz_b} = \sigma^{j-1}_{zz_t}, \quad \mathcal{B}^j_{z_b} = \mathcal{B}^{j-1}_{z_t}, \quad q^j_{z_b} = q^{j-1}_{z_t}, \tag{60}$$

where the subscripts b and t denote the bottom surface of the j-th mathematical layer and the top surface of the adjacent $(j-1)$-th mathematical layer, respectively. By introducing the Navier harmonic expansions in Equations (32)–(36), together with the curvature relations in Equation (6) and the constitutive Equations (11)–(22), the interlaminar continuity conditions can be rewritten in terms of the harmonic amplitudes as follows:

$$U_b^j = U_t^{j-1}, \tag{61}$$

$$V_b^j = V_t^{j-1}, \tag{62}$$

$$W_b^j = W_t^{j-1}, \tag{63}$$

$$\Psi_b^j = \Psi_t^{j-1}, \tag{64}$$

$$\Theta_b^j = \Theta_t^{j-1}, \tag{65}$$

$$\begin{aligned} &\frac{C^j_{55}}{H^j_{\alpha_b}}\bar{\alpha}W^j_b + C^j_{55}U^j_{,z_b} - \frac{C^j_{55}}{H^j_{\alpha_b}R_\alpha}U^j_b + \frac{r^j_{15}}{H^j_{\alpha_b}}\bar{\alpha}\Psi^j_b = \\ &+ \frac{C^{j-1}_{55}}{H^{j-1}_{\alpha_t}}\bar{\alpha}W^{j-1}_t + C^{j-1}_{55}U^{j-1}_{,z_t} - \frac{C^{j-1}_{55}}{H^{j-1}_{\alpha_t}R_\alpha}U^{j-1}_t + \frac{r^{j-1}_{15}}{H^{j-1}_{\alpha_t}}\bar{\alpha}\Psi^{j-1}_t, \end{aligned} \tag{66}$$

$$
\begin{aligned}
&\frac{C_{44}^{j}}{H_{\beta_b}^{j}}\bar{\beta}W_b^{j} + C_{44}^{j}V_{,z_b}^{j} - \frac{C_{44}^{j}}{H_{\beta_b}^{j}R_\beta}V_b^{j} + \frac{r_{24}^{j}}{H_{\beta_b}^{j}}\bar{\beta}\Psi_b^{j} = \\
&+\frac{C_{44}^{j-1}}{H_{\beta_t}^{j-1}}\bar{\beta}W_t^{j-1} + C_{44}^{j-1}V_{,z_t}^{j-1} - \frac{C_{44}^{j-1}}{H_{\beta_t}^{j-1}R_\beta}V_t^{j-1} + \frac{r_{24}^{j-1}}{H_{\beta_t}^{j-1}}\bar{\beta}\Psi_t^{j-1},
\end{aligned}
\tag{67}
$$

$$
\begin{aligned}
&-\frac{C_{13}^{j}}{H_{\alpha_b}^{j}}\bar{\alpha}U_b^{j} + \frac{C_{13}^{j}}{H_{\alpha_b}^{j}R_\alpha}W_b^{j} - \frac{C_{23}^{j}}{H_{\beta_b}^{j}}\bar{\beta}V_b^{j} + \frac{C_{23}^{j}}{H_{\beta_b}^{j}R_\beta}W_b^{j} - \lambda_{33}^{j}\Theta_b^{j} + C_{33}^{j}W_{,z_b}^{j} + r_{33}^{j}\Psi_{,z_b}^{j} = \\
&-\frac{C_{13}^{j-1}}{H_{\alpha_t}^{j-1}}\bar{\alpha}U_t^{j-1} + \frac{C_{13}^{j-1}}{H_{\alpha_t}^{j-1}R_\alpha}W_t^{j-1} - \frac{C_{23}^{j-1}}{H_{\beta_t}^{j-1}}\bar{\beta}V_t^{j-1} + \frac{C_{23}^{j-1}}{H_{\beta_t}^{j-1}R_\beta}W_t^{j-1} - \lambda_{33}^{j-1}\Theta_t^{j-1} + \\
&+C_{33}^{j-1}W_{,z_t}^{j-1} + r_{33}^{j-1}\Psi_{,z_t}^{j-1},
\end{aligned}
\tag{68}
$$

$$
\begin{aligned}
&-\frac{r_{31}^{j}}{H_{\alpha_b}^{j}}\bar{\alpha}U_b^{j} + \frac{r_{31}^{j}}{H_{\alpha_b}^{j}R_\alpha}W_b^{j} - \frac{r_{32}^{j}}{H_{\beta_b}^{j}}\bar{\beta}V_b^{j} + \frac{r_{32}^{j}}{H_{\beta_b}^{j}R_\beta}W_b^{j} + g_3^{j}\Theta_b^{j} + r_{33}^{j}W_{,z_b}^{j} - \mu_{33}^{j}\Psi_{,z_b}^{j} = \\
&-\frac{r_{31}^{j-1}}{H_{\alpha_t}^{j-1}}\bar{\alpha}U_t^{j-1} + \frac{r_{31}^{j-1}}{H_{\alpha_t}^{j-1}R_\alpha}W_t^{j-1} - \frac{r_{32}^{j-1}}{H_{\beta_t}^{j-1}}\bar{\beta}V_t^{j-1} + \frac{r_{32}^{j-1}}{H_{\beta_t}^{j-1}R_\beta}W_t^{j-1} + g_3^{j-1}\Theta_t^{j-1} + \\
&+r_{33}^{j-1}W_{,z_t}^{j-1} - \mu_{33}^{j-1}\Psi_{,z_t}^{j-1},
\end{aligned}
\tag{69}
$$

$$
-k_{33}^{j}\Theta_{,z_b}^{j} = -k_{33}^{j-1}\Theta_{,z_t}^{j-1}. \tag{70}
$$

The explicit interlaminar continuity conditions reported in Equations (61)–(70) can be assembled into the following matrix equation:

$$
\boldsymbol{X}^{j}(0) = \boldsymbol{T}^{j,j-1}\boldsymbol{X}^{j-1}(h_{j-1}), \tag{71}
$$

where $\boldsymbol{T}^{j,j-1}$ is the constant 10×10 transfer matrix relating the state vector at the bottom ($\tilde{z}_j = 0$) of the j-th mathematical layer to the state vector at the top ($\tilde{z}_{j-1} = h_{j-1}$) of the adjacent $(j-1)$-th layer.

By recursively combining the exponential matrix solution in Equation (58) with the transfer relation given in Equation (71), the analytical solution can be propagated through the entire thickness of the multilayered structure. The resulting global relation is

$$
\boldsymbol{X}^{M}(h_M) = \boldsymbol{A}^{**M}\boldsymbol{T}^{M,M-1}\cdots\boldsymbol{T}^{2,1}\boldsymbol{A}^{**1}\boldsymbol{X}^{1}(0) = \boldsymbol{H}_m\boldsymbol{X}^{1}(0), \tag{72}
$$

where $\boldsymbol{H}_m$ is the global transfer matrix obtained by successively assembling the exponential matrices $\boldsymbol{A}^{**j}$ and the transfer matrices $\boldsymbol{T}^{j,j-1}$ corresponding to all the mathematical layers. Regardless of the number of mathematical layers M adopted to discretize the thickness or the Taylor expansion order N employed to evaluate the exponential matrix, $\boldsymbol{H}_m$ always remains a 10×10 matrix. Consequently, the computational effort is significantly reduced while preserving the full three-dimensional description of the multilayered structure. The matrix $\boldsymbol{H}_m$ directly relates the unknown state vector at the bottom surface of the first mathematical layer ($\tilde{z}_1 = 0$) to that at the top surface of the last mathematical layer ($\tilde{z}_M = h_M$).

Simply-supported boundary conditions are adopted along the panel edges since they are the only boundary conditions compatible with the Navier harmonic expansions and therefore allow the derivation of a closed-form analytical solution. For the generic mathematical layer j, the edge boundary conditions are expressed as

$$\begin{aligned} &v^j = 0, \quad w^j = 0, \quad \psi^j = 0, \quad \theta^j = 0, \quad \sigma^j_{\alpha\alpha} = 0 \qquad \text{for} \quad \alpha = 0, a, \\ &u^j = 0, \quad w^j = 0, \quad \psi^j = 0, \quad \theta^j = 0, \quad \sigma^j_{\beta\beta} = 0 \qquad \text{for} \quad \beta = 0, b. \end{aligned} \tag{73}$$

Once the edge boundary conditions have been satisfied, loading boundary conditions must be prescribed at the lower and upper surfaces of the multilayered structure. Depending on the physical problem under investigation, mechanical, magnetic and thermal quantities can be assigned in terms of transverse normal stress, magnetic potential, transverse magnetic induction and over-temperature. Four possible combinations are considered:

$$\sigma_{zz} = \bar{P}_z \sin(\bar{\alpha}\alpha)\sin(\bar{\beta}\beta), \;\; \theta = \bar{\Theta}\sin(\bar{\alpha}\alpha)\sin(\bar{\beta}\beta), \;\; \psi = \bar{\Psi}\sin(\bar{\alpha}\alpha)\sin(\bar{\beta}\beta) \qquad \text{for} \qquad \tilde{z} = 0, h, \tag{74}$$

$$\sigma_{zz} = \bar{P}_z \sin(\bar{\alpha}\alpha)\sin(\bar{\beta}\beta), \;\; \theta = \bar{\Theta}\sin(\bar{\alpha}\alpha)\sin(\bar{\beta}\beta), \;\; \mathcal{B}_z = \bar{\mathcal{B}}_z\sin(\bar{\alpha}\alpha)\sin(\bar{\beta}\beta) \qquad \text{for} \qquad \tilde{z} = 0, h, \tag{75}$$

$$\sigma_{zz} = \bar{P}_z \sin(\bar{\alpha}\alpha)\sin(\bar{\beta}\beta), \;\; q_z = \bar{Q}_z\sin(\bar{\alpha}\alpha)\sin(\bar{\beta}\beta), \;\; \psi = \bar{\Psi}\sin(\bar{\alpha}\alpha)\sin(\bar{\beta}\beta) \qquad \text{for} \qquad \tilde{z} = 0, h, \tag{76}$$

$$\sigma_{zz} = \bar{P}_z \sin(\bar{\alpha}\alpha)\sin(\bar{\beta}\beta), \;\; q_z = \bar{Q}_z\sin(\bar{\alpha}\alpha)\sin(\bar{\beta}\beta), \;\; \mathcal{B}_z = \bar{\mathcal{B}}_z\sin(\bar{\alpha}\alpha)\sin(\bar{\beta}\beta) \qquad \text{for} \qquad \tilde{z} = 0, h. \tag{77}$$

In the previous expressions, the overbar denotes a prescribed boundary value. By substituting the Navier harmonic expansions together with the thermo-magneto-elastic constitutive equations into Equations (74)–(77), the loading boundary conditions can be assembled into the following matrix form:

$$\boldsymbol{B}_b^1 \boldsymbol{X}^1(0) = \boldsymbol{P}_b, \tag{78}$$

$$\boldsymbol{B}_t^M \boldsymbol{X}^M(h_M) = \boldsymbol{P}_t, \tag{79}$$

where $\boldsymbol{B}_b^1$ and $\boldsymbol{B}_t^M$ are the 5×10 loading matrices associated with the bottom surface of the first mathematical layer and the top surface of the last mathematical layer, respectively. Likewise, $\boldsymbol{P}_b$ and $\boldsymbol{P}_t$ are the corresponding 5×1 loading vectors applied at the lower ($\tilde{z} = 0$) and upper ($\tilde{z} = h$) surfaces of the multilayered structure.

By combining Equations (78) and (79) with the global transfer relation given in Equation (72), the final algebraic system becomes

$$\boldsymbol{E}\boldsymbol{X}^1(0) = \boldsymbol{P}, \qquad \textit{where} \qquad \boldsymbol{E} = \begin{bmatrix} \boldsymbol{B}_t^M \boldsymbol{H}_m \\ \boldsymbol{B}_b^1 \end{bmatrix}, \qquad \boldsymbol{P} = \begin{Bmatrix} \boldsymbol{P}_t \\ \boldsymbol{P}_b \end{Bmatrix}. \tag{80}$$

The solution of Equation (80) provides the unknown state vector at the bottom surface of the first mathematical layer. Subsequently, the state vector throughout the thickness can be reconstructed by recursively applying Equations (58) and (71). Once the primary variables have been determined, the secondary variables, namely strains, stresses, magnetic induction components and heat flux components, are readily evaluated from the constitutive and congruence relations reported in Equations (11)–(22) and Equations (23)–(31), respectively.

3. Results

This section presents the numerical results obtained using the proposed 3D layer-wise coupled thermo-magneto-elastic shell model for both flat and curved multilayered structures. Throughout the paper, the formulation is referred to as the 3D-u-θ-ψ model. This designation highlights the main characteristics of the proposed analytical approach, namely a fully three-dimensional formulation (3D) in which the displacement components (u), the over-temperature (θ), and the magnetic potential (ψ) are selected as the primary unknowns.

The Results section is organized into two subsections. The first one is devoted to preliminary assessments, where the proposed 3D-u-θ-ψ model is validated through comparisons with thermo-magneto-elastic solutions available in the literature. These comparisons also allow the identification of suitable values for both the exponential matrix order and the number of mathematical layers required to achieve accurate predictions. The second subsection presents a series of new benchmark results for multilayered plates, cylinders, cylindrical panels, and spherical shells with sandwich configurations and different thickness ratios. The geometries considered throughout this section, together with the corresponding mixed curvilinear orthogonal reference systems, are illustrated in Figure 1.

3.1. Preliminary Results

This subsection presents four preliminary assessments aimed at validating the proposed 3D layer-wise coupled thermo-magneto-elastic shell model (3D-u-θ-ψ). Each assessment has been designed to verify specific features of the formulation by comparison with reference solutions available in the literature.

The first assessment considers a multilayered rectangular plate and is intended to validate the thermo-magneto-elastic coupling together with the material layer and thickness effects for a flat geometry. The second assessment investigates a multilayered spherical shell, extending the validation to curved structures and demonstrating the capability of the proposed model to accurately account for curvature effects in addition to thermo-magneto-elastic coupling and layer-dependent phenomena. These two assessments take into account the full coupling between the thermal, magnetic and elastic field. The third assessment is devoted to a single-layered plate in which only the magneto-elastic coupling is considered, while thermal effects are neglected. This case provides an independent validation of the magnetic formulation as well as the material and thickness effects. Finally, the fourth assessment examines a two-layered square plate in which only the thermo-elastic coupling is retained, whereas magnetic effects are neglected. This last case is employed to validate the thermal formulation together with the corresponding layer-dependent effects.

The last two assessments have been introduced because, to the best of the authors' knowledge, no three-dimensional analytical solutions fully coupling the elastic, magnetic, and thermal fields are currently available in the literature. Consequently, the thermo-elastic and magneto-elastic couplings are validated separately through these benchmark problems.

For the third and fourth assessments, the numerical parameters are fixed to $M = 300$ mathematical layers and a Taylor expansion order $N = 3$ for the exponential matrix, consistently with the convergence analysis previously proposed for three-dimensional static elastic problems by Brischetto [57]. For the first and second assessments, an additional convergence study is reported to justify the adopted values of M and N for the coupled thermo-magneto-elastic problem.

Both the first and the second assessments consider a three-layered *Adaptive Wood/Soft Adaptive Wood/Adaptive Wood* sandwich configuration. The two outer *Adaptive Wood* layers have a thickness equal to $0.3h$, whereas the *Soft Adaptive Wood* core has a thickness of $0.4h$, with h denoting the total thickness of the structure. Both *Adaptive Wood* and *Soft Adaptive Wood* are composite materials obtained by combining wood with barium titanate ($BaTiO_3$) and cobalt ferrite ($CoFe_2O_4$). Their elastic, magnetic, and thermal material properties are summarized in Table 1. Following the convention adopted in the reference solutions of refs. [58,59], the magnetic permeability coefficients μ_{11} and μ_{22} are assumed to be negative in the preliminary assessments. In contrast, positive values will be adopted for the new benchmark problems presented in Section 3.2 in order to better represent the physical behaviour of the material.

Table 1. Thermo-magneto-elastic material properties for preliminary assessments and new benchmarks. Hyphen indicates no occurred value.

	Adaptive Wood [58]	Soft Adaptive Wood [58]	$CoFe_2O_4$ [59]	Cadmium Selenide [60]	PZT-5A [60]
E_1 [GPa]	154.32	77.16	154.32	42.785	61
E_2 [GPa]	154.32	77.16	154.32	42.785	61
E_3 [GPa]	142.83	71.415	142.83	57.707	53.199
ν_{12} [-]	0.36564	0.18282	0.36564	0.4805	0.35
ν_{13} [-]	0.40133	0.200665	0.40133	0.2442	0.38
ν_{23} [-]	0.40133	0.200665	0.40133	0.2442	0.38
G_{12} [GPa]	56.5	28.25	56.5	14.45	22.593
G_{13} [GPa]	45.3	22.65	45.3	13.17	21.1
G_{23} [GPa]	45.3	22.65	45.3	13.17	21.1
μ_{11} [1/K]	14.1×10^{-6}	14.1×10^{-6}	-	1.2566×10^{-6}	1.5005×10^{-6}
μ_{22} [1/K]	14.1×10^{-6}	14.1×10^{-6}	-	1.2566×10^{-6}	1.5005×10^{-6}
μ_{33} [1/K]	7.2×10^{-6}	7.2×10^{-6}	-	1.2566×10^{-6}	1.9989×10^{-6}
k_{11} [N/(mK)]	2.61	1.305	-	9	1.8
k_{22} [N/(mK)]	2.61	1.305	-	9	1.8
k_{33} [N/(mK)]	2.61	1.305	-	13.5	1.8
r_{15} [T]	560	280	550	-	-
r_{24} [T]	560	280	550	-	-
r_{31} [T]	580	290	580.3	-	-
r_{32} [T]	580	290	580.3	-	-
r_{33} [T]	700	350	699.7	-	-
δ_{11} [nH/m]	$\mp 590 \times 10^3$	$\mp 295 \times 10^3$	-590×10^3	-	-
δ_{22} [nH/m]	$\mp 590 \times 10^3$	$\mp 295 \times 10^3$	-590×10^3	-	-
δ_{33} [nH/m]	157×10^3	78.5×10^3	157×10^3	-	-
g_3 [T/K]	6×10^{-3}	3×10^{-3}	-	-	-

In the first preliminary assessment (PA1), a multilayered simply-supported moderately thick rectangular plate is considered. The corresponding geometrical parameters, half-wave numbers, and amplitudes of the prescribed loading boundary conditions are reported in the first column of Table 2. As reference solution, the Equivalent Layer-Wise (ELW) theory developed by Tornabene et al. [58] is adopted. Results from [58] are taken from graphical results by using the open-source software WebPlotDigitizer-4.7.

Table 3 reports the convergence analysis performed on the transverse displacement w, whereas Table 4 compares the results obtained with the proposed 3D-u-θ-ψ model against the reference solution. The convergence study demonstrates that an exponential matrix order equal to $N = 3$ together with $M = 300$ mathematical layers provides fully converged results. Therefore, these values can be regarded as conservative choices, ensuring an accurate evaluation of the thermo-magneto-elastic response.

Table 2. Geometrical data and load boundary conditions for Preliminary Assessments (PA). t indicates the top load impositions at $\tilde{z} = h$ and b indicates the bottom load impositions at $\tilde{z} = 0$. Hyphen indicates no occurred value.

	PA1	PA2	PA3	PA4
a [m]	2	$\frac{1}{6}\pi R_\alpha$	1	1
b [m]	1	$\frac{2}{9}\pi R_\beta$	1	1
R_α [m]	∞	3	∞	∞
R_β [m]	∞	3	∞	∞
h [m]	0.1	0.1	0.3	0.5
m	1	1	1	1
n	1	1	1	1
$\bar{P}_{z_t}$ [Pa]	-7×10^5	-7×10^5	1	0
$\bar{P}_{z_b}$ [Pa]	3×10^5	3×10^5	0	0
$\bar{\Psi}_t$ [A]	-800	-800	-	-

Table 2. *Cont.*

	PA1	PA2	PA3	PA4
$\bar{\Psi}_b$ [A]	20	20	-	-
$\bar{\Theta}_t$ [K]	10	10	-	1
$\bar{\Theta}_b$ [K]	2	2	-	0
$\bar{\mathcal{B}}_{z_t}$ [T]	-	-	0	-
$\bar{\mathcal{B}}_{z_b}$ [T]	-	-	0	-

Table 3. PA1, simply supported three-layered *Adaptive Wood/Soft Adaptive Wood/Adaptive Wood* rectangular plate subjected to thermo-magneto-elastic load conditions. $\tilde{z}/h$ goes from 0 (bottom) to 1 (top). Study convergence on w displacement.

w [10^{-4} m] ($\tilde{z}/h = 1.00$)						
	N = 1	**N = 2**	**N = 3**	**N = 4**	**N = 5**	**N = 6**
M = 10	−1.690	−1.690	−1.690	−1.690	−1.688	−1.688
M = 60	−1.681	−1.680	−1.688	−1.688	−1.688	−1.688
M = 100	−1.681	−1.681	−1.688	−1.688	−1.688	−1.688
M = 160	−1.681	−1.681	−1.688	−1.688	−1.688	−1.688
M = 200	−1.681	−1.688	−1.688	−1.688	−1.688	−1.688
M = 260	−1.681	−1.688	−1.688	−1.688	−1.688	−1.688
M = 300	−1.681	−1.688	−1.688	−1.688	−1.688	−1.688

Table 4. PA1, simply supported three-layered *Adaptive Wood/Soft Adaptive Wood/Adaptive Wood* rectangular plate subjected to thermo-magneto-elastic load conditions. $\tilde{z}/h$ goes from 0 (bottom) to 1 (top).

		ELW [58]	3D-u-θ-ψ	Percentage Error [%]
u [10^{-6} m]	($\tilde{z}/h = 0.50$)	−7.682	−7.729	−0.608
v [10^{-5} m]	($\tilde{z}/h = 0.30$)	−2.487	−2.496	−0.362
w [10^{-4} m]	($\tilde{z}/h = 1.00$)	−1.689	−1.688	0.059
ψ [10^{2} A]	($\tilde{z}/h = 0.50$)	−2.078	−2.110	−1.540
θ [K]	($\tilde{z}/h = 0.70$)	4.109	4.110	−0.024
$\sigma_{\alpha\alpha}$ [10^{7} Pa]	($\tilde{z}/h = 1.00$)	−2.103	−2.109	−0.285
$\sigma_{\beta z}$ [10^{6} Pa]	($\tilde{z}/h = 0.50$)	−1.827	−1.828	−0.055
σ_{zz} [10^{5} Pa]	($\tilde{z}/h = 0.50$)	−1.036	−1.010	2.510
$\mathcal{B}_{\alpha}$ [10^{-1} T]	($\tilde{z}/h = 0.50$)	−1.062	−1.079	−1.576
q_z [10^{1} W/m^2]	($\tilde{z}/h = 0.00$)	−7.208	−7.202	0.083

The reference values reported in Table 4 were extracted from the through-the-thickness distributions presented by Tornabene et al. [58] at the in-plane coordinates $\alpha = 0.25a$ and $\beta = 0.25b$. An excellent agreement is observed between the proposed formulation and the reference model for all the investigated quantities, including displacement components, magnetic potential, over-temperature, in-plane normal stress, transverse shear stress, transverse normal stress, in-plane normal magnetic induction, and transverse normal heat flux. The comparison confirms the accuracy of the proposed 3D-u-θ-ψ model and its capability to correctly capture the thermo-magneto-elastic coupling together with the material layer and thickness effects in multilayered plate structures.

For the second preliminary assessment (PA2), a multilayered simply-supported moderately thick spherical shell is investigated. The corresponding geometrical parameters, half-wave numbers, and prescribed loading boundary conditions are reported in the second column of Table 2. As in PA1, the reference solution is provided by the Equivalent Layer-Wise (ELW) theory developed by Tornabene et al. [58].

Table 5 presents the convergence analysis performed on the transverse displacement w for the spherical shell configuration. Also for this curved geometry, an exponential matrix order equal to $N = 3$ combined with $M = 300$ mathematical layers provides converged results. A slightly slower convergence is observed with respect to the plate case because of the additional curvature terms appearing in the governing equations. Nevertheless, the selected values of N and M guarantee an accurate evaluation of the thermo-magneto-elastic response.

The reference values listed in Table 6 were extracted from the through-the-thickness distributions reported by Tornabene et al. [58] at the in-plane coordinates $\alpha = 0.25a$ and $\beta = 0.25b$. An excellent agreement is achieved for the in-plane and transverse displacement components, magnetic potential, over-temperature, transverse shear and transverse normal stresses, in-plane normal stress, and in-plane normal magnetic induction. These comparisons validate the capability of the proposed 3D-u-θ-ψ model to accurately reproduce the thermo-magneto-elastic coupling together with the material layer, thickness, and curvature effects in multilayered spherical shells.

Table 5. PA2, simply supported three-layered *Adaptive Wood/Soft Adaptive Wood/Adaptive Wood* spherical subjected to thermo-magneto-elastic load conditions. $\tilde{z}/h$ goes from 0 (bottom) to 1 (top). Study convergence on σ_{zz} stress.

	σ_{zz} [10^4 Pa] ($\tilde{z}/h = 0.50$)					
	N = 1	**N = 2**	**N = 3**	**N = 4**	**N = 5**	**N = 6**
M = 10	5.918	8.191	8.144	8.144	8.144	8.144
M = 60	7.803	8.148	8.147	8.147	8.147	8.147
M = 100	7.942	8.147	8.147	8.147	8.147	8.147
M = 160	8.019	8.147	8.147	8.147	8.147	8.147
M = 200	8.045	8.147	8.147	8.147	8.147	8.147
M = 260	8.069	8.147	8.147	8.147	8.147	8.147
M = 300	8.079	8.147	8.147	8.147	8.147	8.147

Table 6. PA2, simply supported three-layered *Adaptive Wood/Soft Adaptive Wood/Adaptive Wood* spherical shell subjected to thermo-magneto-elastic load conditions. $\tilde{z}/h$ goes from 0 (bottom) to 1 (top).

		ELW [58]	**3D-u-θ-ψ**	**Percentage Error [%]**
u [10^{-5} m]	($\tilde{z}/h = 0.50$)	−3.907	−3.910	−0.077
v [10^{-5} m]	($\tilde{z}/h = 0.30$)	−3.278	−3.289	−0.336
w [10^{-4} m]	($\tilde{z}/h = 1.00$)	−1.302	−1.300	0.153
ψ [10^2 A]	($\tilde{z}/h = 0.50$)	−2.056	−2.074	−0.875
θ [K]	($\tilde{z}/h = 0.70$)	4.138	4.126	0.290
$\sigma_{\alpha\alpha}$ [10^7 Pa]	($\tilde{z}/h = 1.00$)	−1.665	−1.667	−0.120
$\sigma_{\beta z}$ [10^5 Pa]	($\tilde{z}/h = 0.50$)	−4.997	−5.042	−0.901
σ_{zz} [10^4 Pa]	($\tilde{z}/h = 0.50$)	8.296	8.147	1.796
$\mathcal{B}_\alpha$ [10^{-1} T]	($\tilde{z}/h = 0.50$)	−1.250	−1.293	−3.440

The small discrepancies observed in Tables 4 and 6 mainly arise from the fact that the ELW reference values were extracted from the graphical distributions reported by Tornabene et al. [58]. Consequently, the tabulated reference data are affected by the unavoidable approximations associated with the graphical reading procedure.

For the third preliminary assessment (PA3), a single-layered simply-supported thick square plate made of $CoFe_2O_4$ is considered under open-circuit magnetic boundary conditions. In this configuration, the loading conditions are prescribed by imposing the transverse magnetic induction components $\mathcal{B}_{z_t}$ and $\mathcal{B}_{z_b}$ at the top and bottom surfaces, respectively. The corresponding geometrical parameters, half-wave numbers, and prescribed loading boundary conditions are reported in the third column of Table 2, whereas the material properties of $CoFe_2O_4$ are summarized in Table 1. As reference solution, the three-dimensional magneto-elastic model developed by Heyliger and Pan [59] is adopted.

The comparison is carried out at different through-the-thickness locations $\tilde{z}/h$. As shown in Table 7, the proposed 3D-u-θ-ψ model exhibits an excellent agreement with the reference solution in terms of in-plane displacement, transverse displacement, and magnetic potential. Since thermal effects are neglected in this assessment, the obtained results provide an independent validation of the magneto-elastic coupling together with the capability of the proposed formulation to accurately reproduce the material layer and thickness effects.

Table 7. PA3, simply-supported single-layered $CoFe_2O_4$ square plate subjected to magneto-elastic load conditions. $\tilde{z}/h$ goes from 0 (bottom) to 1 (top).

		3D [59]	**3D-u-θ-ψ**	**Percentage Error [%]**
$u\,[10^{-11}\text{ m}]$	$(\tilde{z}/h = 0.000)$	0.31968	0.31968	0.000
$u\,[10^{-11}\text{ m}]$	$(\tilde{z}/h = 0.167)$	0.10782	0.10782	0.000
$u\,[10^{-11}\text{ m}]$	$(\tilde{z}/h = 0.567)$	−0.04676	−0.04676	0.000
$u\,[10^{-11}\text{ m}]$	$(\tilde{z}/h = 1.000)$	−0.27657	−0.27657	0.000
$w\,[10^{-11}\text{ m}]$	$(\tilde{z}/h = 0.000)$	0.92335	0.92335	0.000
$w\,[10^{-11}\text{ m}]$	$(\tilde{z}/h = 0.167)$	1.0076	1.0075	0.010
$w\,[10^{-11}\text{ m}]$	$(\tilde{z}/h = 0.567)$	1.0378	1.0378	0.000
$w\,[10^{-11}\text{ m}]$	$(\tilde{z}/h = 1.000)$	1.0112	1.0112	0.000
$\psi\,[10^{-5}\text{ A}]$	$(\tilde{z}/h = 0.000)$	−0.51965	−0.51967	0.004
$\psi\,[10^{-5}\text{ A}]$	$(\tilde{z}/h = 0.167)$	−0.49108	−0.49108	0.000
$\psi\,[10^{-5}\text{ A}]$	$(\tilde{z}/h = 0.567)$	−0.26590	−0.26589	0.004
$\psi\,[10^{-5}\text{ A}]$	$(\tilde{z}/h = 1.000)$	0.00400	0.00398	0.500

The fourth preliminary assessment (PA4) considers a two-layered simply-supported thick plate with a *Cadmium Selenide/PZT-5A* configuration. The corresponding geometrical parameters, half-wave numbers, and prescribed loading boundary conditions are reported in the fourth column of Table 2, whereas the material properties of *Cadmium Selenide* and *PZT-5A* are summarized in Table 1. As reference solution, the three-dimensional Sampling Surface (SaS) method proposed by Kulikov and Plotnikova [60] is employed. The comparison is carried out at different through-the-thickness locations $\tilde{z}/h$ for the following dimensionless variables:

$$\bar{u} = \frac{10u}{a\alpha_0\Theta_t}; \;\; \bar{w} = \frac{100w}{\frac{a}{h}a\alpha_0\Theta_t}; \;\; \bar{\theta} = \frac{\theta}{\Theta_t}; \;\; \bar{\sigma}_{\alpha\alpha} = \frac{10\sigma_{\alpha\alpha}}{E_1\alpha_0\Theta_t}; \;\; \bar{\sigma}_{\alpha\beta} = \frac{10\sigma_{\alpha\beta}}{E_1\alpha_0\Theta_t}; \tag{81}$$

$$\bar{\sigma}_{\alpha z} = \frac{10\frac{a}{h}\sigma_{\alpha z}}{E_1\alpha_0\Theta_t}; \;\; \bar{\sigma}_{zz} = \frac{10(\frac{a}{h})^2\sigma_{zz}}{E_1\alpha_0\Theta_t}; \;\; \bar{q}_z = \frac{10aq_z}{\frac{a}{h}k_0\Theta_t}. \tag{82}$$

Θ_t denotes the prescribed over-temperature at the top surface of the structure, $k_0 = 9\,\text{W/mK}$, $\alpha_0 = 4.396 \times 10^{-6}\,1/\text{K}$, and E_1 is the Young's modulus of *Cadmium Selenide* expressed in Pascal. As shown in Table 8, the proposed 3D-u-θ-ψ model exhibits an excellent agreement with the three-dimensional reference solution for all the normalized variables considered. These results provide a further validation of the proposed formulation, confirming its capability to accurately capture the thermo-elastic coupling together with the material layer and thickness effects.

Table 8. PA4, simply supported two-layered *Cadmium Selenide/PZT-5A* plate subjected to thermo-elastic load conditions. $\tilde{z}/h$ goes from 0 (bottom) to 1 (top).

		3D [60]	**3D-u-θ-ψ**	**Percentage Error [%]**
$\bar{u}$	$(\tilde{z}/h = 1.00)$	-2.3801	-2.3811	-0.042
$\bar{w}$	$(\tilde{z}/h = 1.00)$	10.215	10.243	-0.274
θ	$(\tilde{z}/h = 0.00)$	0.6058	0.6058	0.000
$\sigma_{\alpha\alpha}$	$(\tilde{z}/h = 1.00)$	-4.6432	-4.6372	0.130
$\sigma_{\alpha\beta}$	$(\tilde{z}/h = 1.00)$	-5.0506	-5.0528	-0.044
$\sigma_{\alpha z}$	$(\tilde{z}/h = 0.00)$	1.3501	1.3384	0.867
σ_{zz}	$(\tilde{z}/h = 0.00)$	-1.6477	-1.6388	0.540
q_z	$(\tilde{z}/h = 0.00)$	-3.3465	-3.3465	0.000

Thanks to these four preliminary assessments, all the key features involved in the thermo-magneto-elastic response of both flat and curved multilayered structures have been successfully validated. In particular, the proposed 3D-u-θ-ψ model accurately captures the material layer effect, the thickness effect, the thermo-magneto-elastic coupling, and the influence of structural curvature. The validation procedure has been carried out by adopting $M = 300$ mathematical layers and an exponential matrix order equal to $N = 3$. The convergence studies reported in Tables 3–5 demonstrate that these values provide fully converged solutions for both flat and curved geometries. Consequently, the same numerical parameters ($M = 300$ and $N = 3$) are employed in the four new benchmark cases presented in the following subsection.

3.2. New Results

This subsection presents four new benchmark problems involving a sandwich plate, a cylinder, a cylindrical panel, and a spherical shell. According to the convergence analyses discussed in the previous subsection, all the results are obtained by adopting an exponential matrix order equal to $N = 3$ and $M = 300$ mathematical layers.

All the investigated structures consider an *Adaptive Wood/Soft Adaptive Wood/Adaptive Wood* sandwich configuration. Each outer *Adaptive Wood* layer has a thickness equal to 0.1, whereas the *Soft Adaptive Wood* core has a thickness of $0.8h$, with h denoting the total thickness of the multilayered structure. The corresponding elastic, magnetic, and thermal material properties are listed in Table 1. Unlike the preliminary assessments, the magnetic permeability coefficients μ_{11} and μ_{22} are assumed to be positive, consistently with the physical interpretation proposed by Pan [61].

Two different loading boundary configurations are considered. Both configurations prescribe the over-temperature at the outer surfaces, whereas the magnetic loading is assigned either in terms of magnetic potential or transverse magnetic induction. The two loading boundary conditions (LB) are defined as follows:

$$LB1: \quad \bar{\Theta}_t = 1.5\,K, \quad \bar{\Theta}_b = 0\,K; \qquad \bar{\Psi}_t = 10\,A, \quad \bar{\Psi}_b = 0\,A, \tag{83}$$

$$LB2: \quad \bar{\Theta}_t = 1.5\,K, \quad \bar{\Theta}_b = 0\,K; \qquad \bar{\mathcal{B}}_{z_t} = 1\,T, \quad \bar{\mathcal{B}}_{z_b} = 0\,T. \tag{84}$$

Subscripts b and t denote the bottom and top surfaces of the multilayered structure, respectively.

For each benchmark problem, eight representative variables are reported in tabular form at selected through-the-thickness locations $\tilde{z}/h$ and for different thickness ratios. In addition, through-the-thickness distributions are presented for a representative thickness ratio under both loading boundary configurations in order to illustrate the main characteristics of the thermo-magneto-elastic response.

In the first new case (NC1), a sandwich square plate is investigated. The corresponding geometrical parameters and half-wave numbers are reported in the first column of Table 9. Tables 10 and 11 collect representative results for the two loading boundary configurations by considering the variables u (or v), w, ψ, θ, $\mathcal{B}_z$, q_z, $\sigma_{\alpha\beta}$, $\sigma_{\beta\beta}$, and σ_{zz} at selected $\tilde{z}/h$ locations and for different thickness ratios.

As the slenderness ratio a/h increases, both the transverse displacement w and the over-temperature θ increase because of the progressive reduction in the structural stiffness. The magnetic potential ψ exhibits a sign change for the LB1 configuration at $\tilde{z}/h = 0.25$, whereas it remains negative for the LB2 configuration at $\tilde{z}/h = 0.75$, owing to the prescribed transverse magnetic induction that maintains the magnetic field oriented along the negative direction. A similar behaviour is observed for the transverse magnetic induction $\mathcal{B}_z$, which changes from positive to negative values under the LB1 configuration ($\tilde{z}/h = 1.00$), while remaining positive for the LB2 configuration ($\tilde{z}/h = 0.75$). Conversely, the transverse heat flux q_z assumes identical values for both loading configurations, indicating that the imposed magnetic boundary conditions do not influence the heat transfer through the thickness.

Figures 2 and 3 report the through-the-thickness distributions of the selected variables for representative thickness ratios ($a/h = 4$ for LB1 and $a/h = 10$ for LB2). The zigzag behaviour associated with the multilayered configuration is clearly visible through the slope changes occurring at each physical interface. Moreover, all the proposed variables satisfy the interlaminar continuity conditions, as no discontinuities are observed across the interfaces. The two load boundary conditions show an opposite trend for what concerns magnetic potential and transverse magnetic induction. For the LB1 load boundary condition the applied magnetic potential is a monotonous trend while the transverse magnetic induction component is non-monotonous as it is a response variable. This specific trend for the $\mathcal{B}_z$ component happens due to the sandwich layer inhomogeneity. In the LB2 load boundary configuration, the monotonous trend is the transverse magnetic induction component while the response variable is the magnetic potential. For this case, the magnetic response is mainly concentrated in the soft core of the sandwich configuration. It must be also noted that the transverse heat flux q_{t_z} has the same trend for both the load boundary conditions. The trend shows a peak heat lose placed at the bottom of the plate. The two different transverse heat flux trends are due to the pyromagnetic coefficient. The q_{t_z} trend curve in Figure 2 is due to the strong gradient influencing the pyromagnetic effect.

The prescribed loading boundary conditions are correctly recovered at the outer surfaces. In the LB1 configuration, the over-temperature varies from 1.5 K at the top surface to 0 K at the bottom surface, while the magnetic potential decreases from 10 A to 0 A. In the LB2 configuration, the same thermal distribution is obtained, whereas the transverse magnetic induction varies from 1 T at the top surface to 0 T at the bottom surface. Since no external mechanical pressure is applied, the transverse normal stress σ_{zz} is equal to zero at both outer surfaces for the two loading configurations.

Overall, the proposed benchmark clearly highlights the capability of the present formulation to accurately capture the thermo-magneto-elastic coupling together with the material layer effect, the thickness effect, the zigzag behaviour, and the correct fulfillment of both boundary and interlaminar continuity conditions.

Table 9. Geometrical data and half-wave numbers for the New Cases (NC).

	NC1	NC2	NC3	NC4
a [m]	1	$2\pi R_\alpha$	$\frac{\pi}{3}R_\alpha$	$\frac{\pi}{3}R_\alpha$
b [m]	1	10	2	$\frac{\pi}{3}R_\alpha$
R_α [m]	∞	10	10	10
R_β [m]	∞	∞	∞	10
m	1	2	1	1
n	1	1	0	1

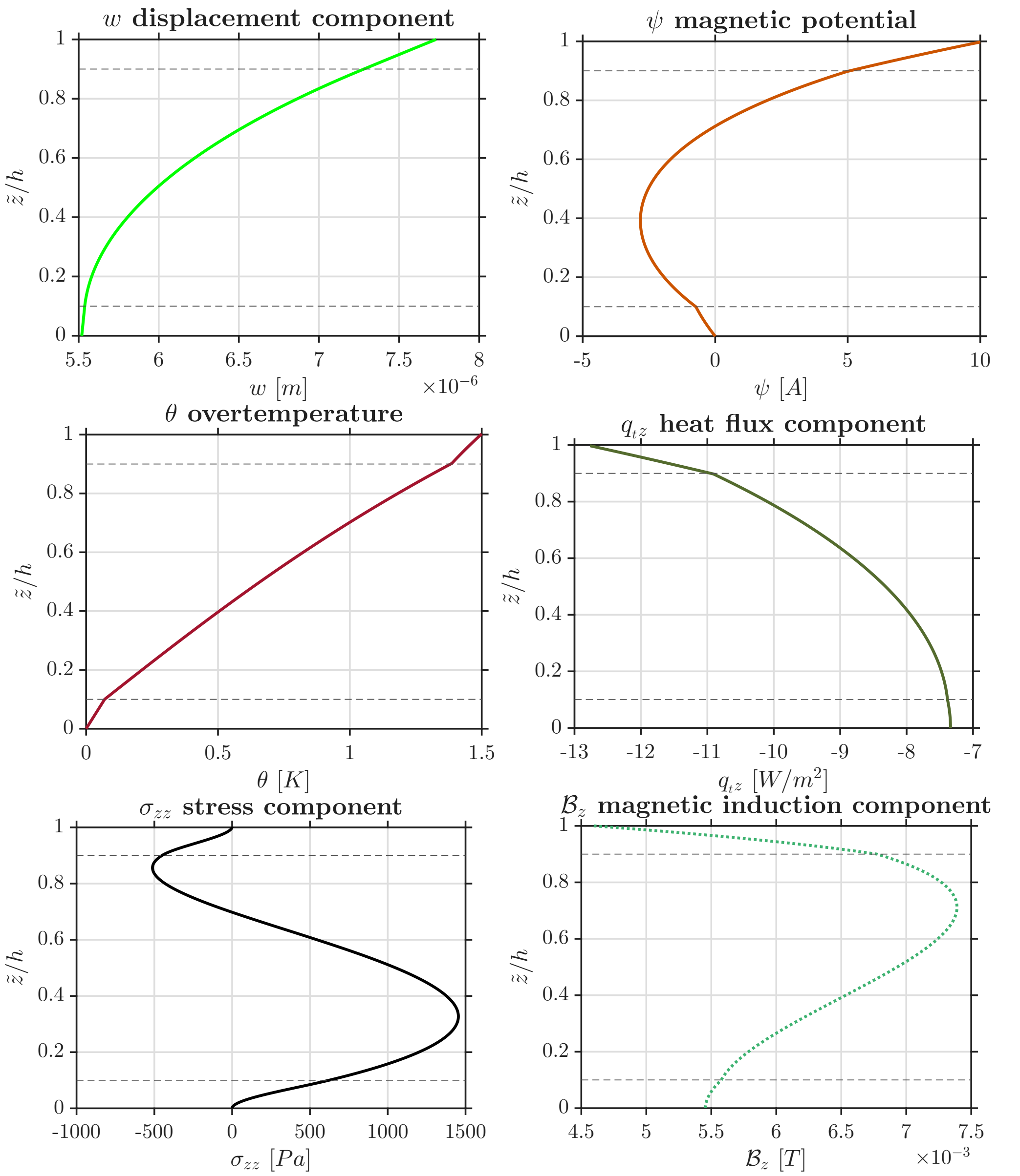

Figure 2. NC1: simply-supported sandwich *Adaptive Wood/Soft Adaptive Wood/Adaptive Wood* square plate considering LB1 Load Boundary conditions ($\psi_t = 10\,\mathrm{V}$, $\psi_b = 0\,\mathrm{V}$ and $\theta_t = 1.5\,\mathrm{K}$, $\theta_b = 0\,\mathrm{K}$). Thickness ratio is $a/h = 4$. Results are obtained via the 3D-u-θ-ψ model.

In the second new case (NC2), a sandwich cylinder is considered. The corresponding geometrical parameters and half-wave numbers are reported in the second column of Table 9. Table 12 presents the variables v, w, ψ, θ, $\mathcal{B}_z$, q_z, $\sigma_{\beta\beta}$, and σ_{zz} at selected $\tilde{z}/h$ locations for thickness ratios ranging from $R_\alpha/h = 2$ to $R_\alpha/h = 100$ under the LB1 loading configuration. Similarly, Table 13 reports u, w, ψ, θ, $\mathcal{B}_z$, q_z, $\sigma_{\alpha\alpha}$, and σ_{zz} for the LB2 configuration.

Table 10. NC1, simply supported sandwich *Adaptive Wood/Soft Adaptive Wood/Adaptive Wood* square plate considering LB1 load boundary conditions. Results are obtained via the 3D-u-θ-ψ model. $\tilde{z}/h$ goes from 0 (bottom) to 1 (top).

a/h	2	4	10	50	100
			u [10^{-7} m] ($\tilde{z}/h = 0.25$)		
	−6.0758	−9.2130	−10.390	−10.188	−9.6284
			w [10^{-6} m] ($\tilde{z}/h = 0.50$)		
	2.7086	5.9892	15.411	77.633	155.36
			ψ [10^{-3} A] ($\tilde{z}/h = 0.25$)		
	−2659.9	−2328.0	8.5258	1783.0	2004.2
			θ [10^{-1} K] ($\tilde{z}/h = 0.75$)		
	9.2028	10.911	11.537	11.661	11.665
			$\mathcal{B}_z$ [10^{-4} T] ($\tilde{z}/h = 1.00$)		
	68.431	45.957	1.2899	−337.36	−776.37
			q_z [10^{1} W/m^2] ($\tilde{z}/h = 1.00$)		
	−1.1582	−1.2766	−2.3444	−10.909	−21.767
			$\sigma_{\alpha\beta}$ [10^{5} Pa] ($\tilde{z}/h = 0.50$)		
	−2.6967	−3.6419	−3.9823	−3.9735	−3.8753
			σ_{zz} [Pa] ($\tilde{z}/h = 0.75$)		
	3794.9	−260.10	−129.75	−3.0823	0.0937

Table 11. NC1, simply supported sandwich *Adaptive Wood/Soft Adaptive Wood/Adaptive Wood* square plate considering LB2 load boundary conditions. Results are obtained via the 3D-u-θ-ψ model. $\tilde{z}/h$ goes from 0 (bottom) to 1 (top).

a/h	2	4	10	50	100
			v [10^{-7} m] ($\tilde{z}/h = 0.25$)		
	−6.6033	−11.942	−14.264	−14.750	−14.766
			w [10^{-6} m] ($\tilde{z}/h = 0.75$)		
	7.1900	14.583	36.137	179.71	359.35
			ψ [10^{2} A] ($\tilde{z}/h = 0.75$)		
	−3.8754	−7.4552	−15.357	−70.997	−141.59
			θ [10^{-1} K] ($\tilde{z}/h = 0.50$)		
	4.7777	6.6215	7.3471	7.4938	7.4984
			$\mathcal{B}_z$ [10^{-2} T] ($\tilde{z}/h = 0.25$)		
	3.3132	13.691	25.315	28.996	29.124
			q_z [10^{1} W/m^2] ($\tilde{z}/h = 1.00$)		
	−1.1582	−1.2766	−2.3444	−10.909	−21.767
			$\sigma_{\beta\beta}$ [10^{6} Pa] ($\tilde{z}/h = 1.00$)		
	−2.7559	−2.2011	−1.6838	−1.5304	−1.5251
			σ_{zz} [10^{3} Pa] ($\tilde{z}/h = 0.50$)		
	106.38	16.311	−0.3789	−0.0550	−0.0141

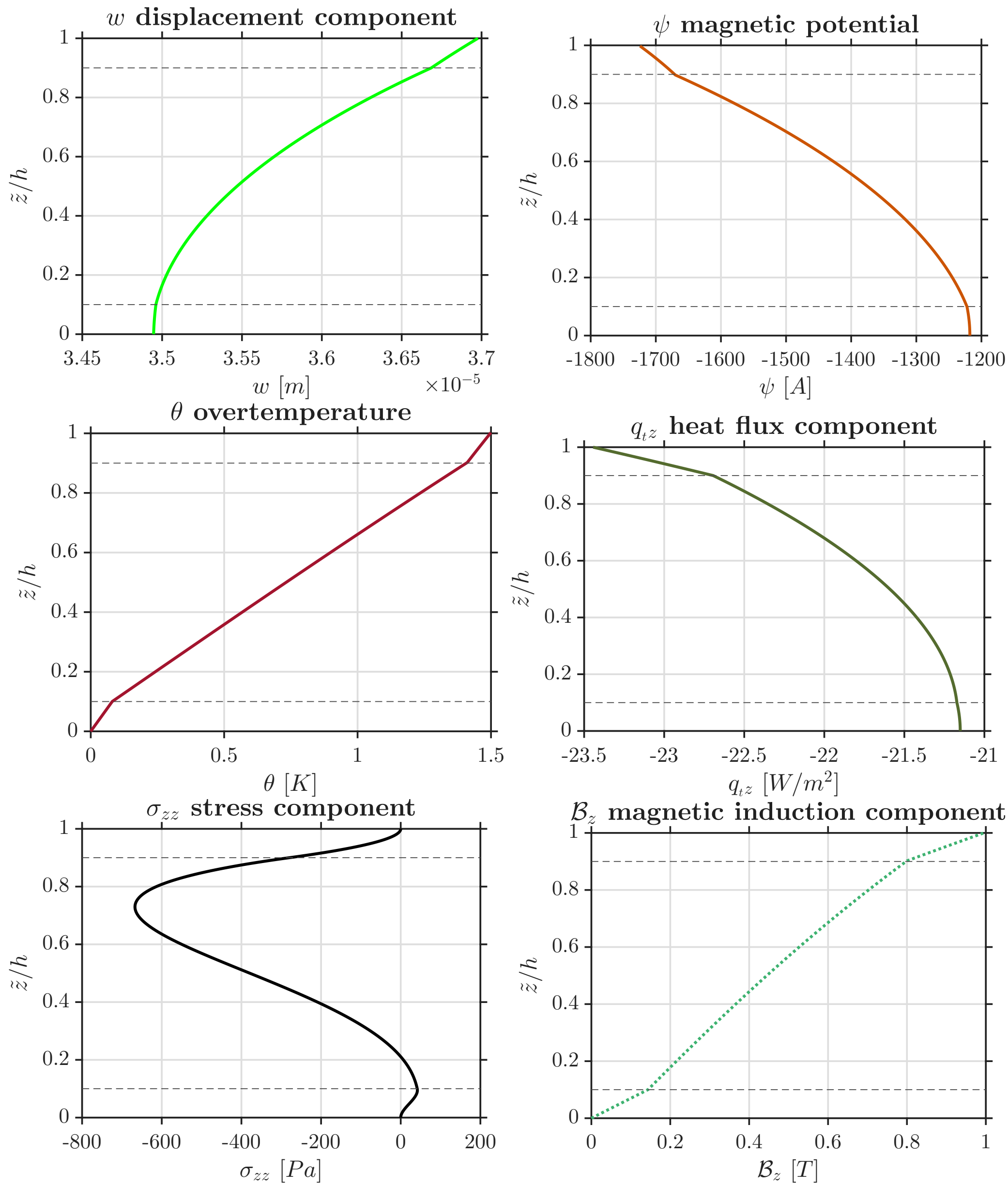

Figure 3. NC1: simply-supported sandwich *Adaptive Wood/Soft Adaptive Wood/Adaptive Wood* square plate considering LB2 Load Boundary conditions ($\mathcal{B}_{z_t} = 1\,\mathrm{T}$, $\mathcal{B}_{z_b} = 0\,\mathrm{T}$ and $\theta_t = 1.5\,\mathrm{K}$, $\theta_b = 0\,\mathrm{K}$). Thickness ratio is $a/h = 10$. Results are obtained via the 3D-u-θ-ψ model.

For both loading configurations, the variation of the transverse displacement w with the thickness ratio is not monotonic because of the curvature effect associated with the cylindrical geometry. The magnetic loading strongly influences the magnetic variables. Under the LB1 configuration, the magnetic potential ψ changes sign from negative values for thick cylinders to positive values for thin cylinders ($\tilde{z}/h = 0.25$), whereas it remains negative for all thickness ratios under the LB2 configuration ($\tilde{z}/h = 0.75$). This behaviour is associated with the different magnetic boundary conditions: under LB1 the magnetic potential reverses its distribution through the thickness as the cylinder becomes thinner, whereas under LB2 its direction remains unchanged. Conversely, the transverse magnetic induction $\mathcal{B}_z$ remains positive for both loading configurations. It decreases with increasing R_α/h under LB1 ($\tilde{z}/h = 1.00$), whereas it increases under LB2 ($\tilde{z}/h = 0.25$). The transverse heat flux q_z assumes identical values for the two loading configurations, confirming that the prescribed magnetic boundary conditions do not affect the heat transfer through the thickness.

Table 12. NC2, simply supported sandwich *Adaptive Wood/Soft Adaptive Wood/Adaptive Wood* cylinder considering LB1 load boundary conditions. Results are obtained via the 3D-u-θ-ψ model. $\tilde{z}/h$ goes from 0 (bottom) to 1 (top).

R_α/h	2	4	10	50	100
			v $[10^{-6}$ m$]$ $(\tilde{z}/h = 0.25)$		
	−5.3584	−9.6192	−20.452	−31.041	−32.253
			w $[10^{-5}$ m$]$ $(\tilde{z}/h = 0.50)$		
	6.9796	11.057	13.611	12.385	11.991
			ψ $[10^{-1}$ A$]$ $(\tilde{z}/h = 0.25)$		
	−477.19	−422.60	−177.82	−16.207	3.1459
			θ [K] $(\tilde{z}/h = 0.75)$		
	1.0161	1.1238	1.1595	1.1664	1.1666
			$\mathcal{B}_z$ $[10^{-3}$ T$]$ $(\tilde{z}/h = 1.00)$		
	15.277	12.167	10.554	6.9899	2.5793
			q_z $[10^{-1}$ W/m$^2]$ $(\tilde{z}/h = 1.00)$		
	−8.5138	−10.960	−22.681	−108.94	−217.59
			$\sigma_{\beta\beta}$ $[10^3$ Pa$]$ $(\tilde{z}/h = 0.50)$		
	40.048	39.857	37.127	10.489	5.5868
			σ_{zz} $[10^3$ Pa$]$ $(\tilde{z}/h = 0.75)$		
	108.45	56.178	28.034	7.1475	3.6876

Figures 4 and 5 show the through-the-thickness distributions of the selected variables for representative thickness ratios. In both cases, the zigzag behaviour is clearly visible through the slope discontinuities at the material interfaces, while all variables remain continuous across the interfaces, confirming the correct enforcement of the interlaminar continuity conditions. By comparing the two different Figures 4 and 5 the w trend for the LB2 condition is strongly non-monotonous due to the flexural-membranal coupling present in the cylinder structures. This is due to the fact that a free magnetic potential component creates a much more irregular magnetostrictive effect, amplifying the mechanical oscillations along the thickness direction. In addition, the transverse heat flux for the LB1 configuration is more intense rather than the transverse heat flux for the LB2 configuration as thinner thickness has to withstand the same heat load.

The prescribed loading boundary conditions are correctly satisfied at the outer surfaces. In Figure 4, this is demonstrated by the magnetic potential ψ and over-temperature θ distributions, whereas in Figure 5 $\mathcal{B}_z$ and θ recover the imposed boundary values. Since no external mechanical pressure is applied, the transverse normal stress σ_{zz} vanishes at both outer surfaces of the cylinder. Overall, the proposed benchmark confirms the capability of the present formulation to accurately reproduce the thermo-magneto-elastic coupling together with the curvature effect, the material layer effect, the thickness effect, the zigzag behaviour, and the interlaminar continuity conditions.

The third new case (NC3) is devoted to a sandwich cylindrical panel. The corresponding geometrical parameters and half-wave numbers are reported in the third column of Table 9. Tables 14 and 15 collect representative results for the two loading boundary configurations by considering the variables u, w, ψ, θ, $\mathcal{B}_z$, q_z, $\sigma_{\alpha\alpha}$, and σ_{zz} at selected $\tilde{z}/h$ locations and for different thickness ratios.

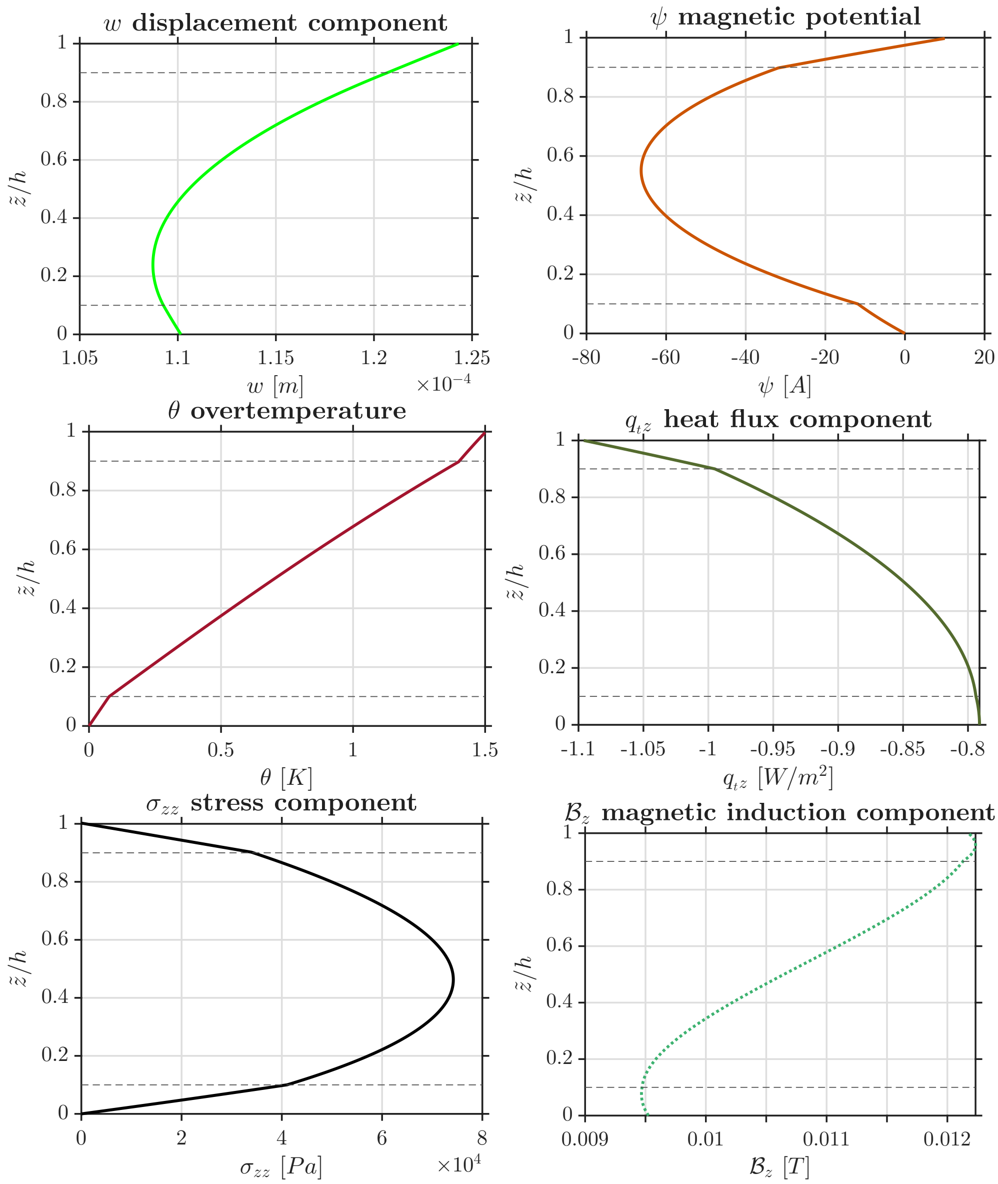

Figure 4. NC2: simply-supported sandwich *Adaptive Wood/Soft Adaptive Wood/Adaptive Wood* cylinder considering LB1 Load Boundary conditions ($\psi_t = 10\,\mathrm{V}$, $\psi_b = 0\,\mathrm{V}$ and $\theta_t = 1.5\,\mathrm{K}$, $\theta_b = 0\,\mathrm{K}$). Thickness ratio is $R_\alpha/h = 4$. Results are obtained via the 3D-u-θ-ψ model.

Table 13. NC2, simply supported sandwich *Adaptive Wood/Soft Adaptive Wood/Adaptive Wood* cylinder considering LB2 load boundary conditions. Results are obtained via the 3D-u-θ-ψ model. $\tilde{z}/h$ goes from 0 (bottom) to 1 (top).

R_α/h	2	4	10	50	100
			$u\,[10^{-5}\,\mathrm{m}]$ $(\tilde{z}/h = 0.25)$		
	1.7567	1.8248	−0.1791	−12.313	−25.930
			$w\,[10^{-5}\,\mathrm{m}]$ $(\tilde{z}/h = 0.75)$		
	12.777	18.834	19.452	5.2599	−7.3954
			$\psi\,[10^{3}\,\mathrm{A}]$ $(\tilde{z}/h = 0.75)$		
	−7.3437	−12.697	−27.008	−128.73	−257.03
			$\theta\,[10^{-1}\,\mathrm{K}]$ $(\tilde{z}/h = 0.50)$		
	5.7753	6.9961	7.4153	7.4966	7.4991

Table 13. *Cont.*

R_α/h	2	4	10	50	100
			$\mathcal{B}_z$ $[10^{-2}$ T] $(\tilde{z}/h = 0.25)$		
	7.3616	18.996	27.158	29.115	29.164
			q_z $[10^{-1}$ W/m$^2]$ $(\tilde{z}/h = 1.00)$		
	−8.5138	−10.960	−22.681	−108.94	−217.59
			$\sigma_{\alpha\alpha}$ $[10^6$ Pa] $(\tilde{z}/h = 1.00)$		
	−2.2128	−1.6248	−2.2636	−3.6515	−3.8640
			σ_{zz} $[10^3$ Pa] $(\tilde{z}/h = 0.50)$		
	219.21	116.20	63.652	15.414	7.8430

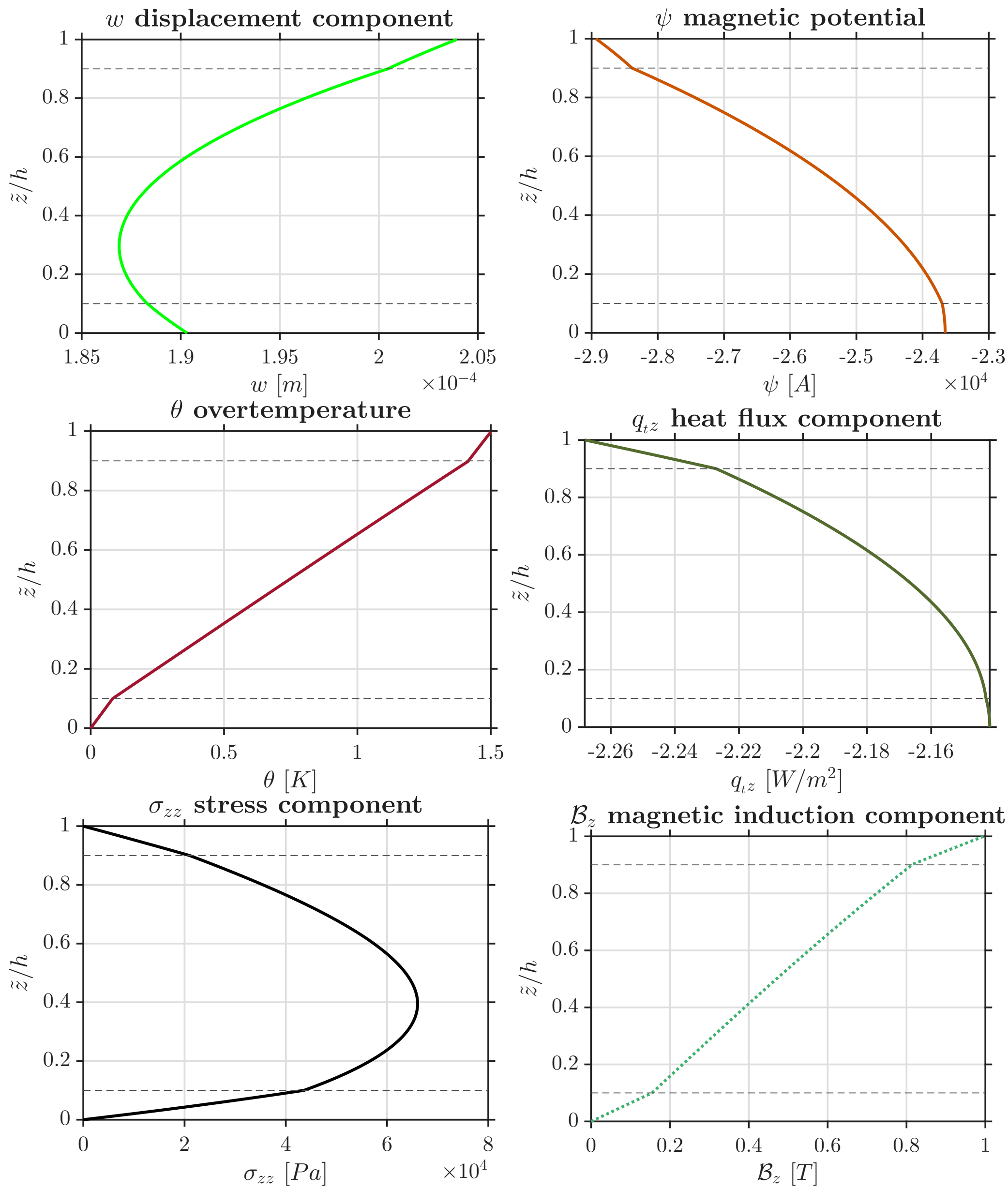

Figure 5. NC2: simply-supported sandwich *Adaptive Wood/Soft Adaptive Wood/Adaptive Wood* cylinder considering LB2 Load Boundary conditions ($\mathcal{B}_{z_t} = 1$ T, $\mathcal{B}_{z_b} = 0$ T and $\theta_t = 1.5$ K, $\theta_b = 0$ K). Thickness ratio is $R_\alpha/h = 10$. Results are obtained via the 3D-u-θ-ψ model.

Table 14. NC3, simply supported sandwich *Adaptive Wood/Soft Adaptive Wood/Adaptive Wood* cylindrical shell panel considering LB1 load boundary conditions. Results are obtained via the 3D-u-θ-ψ model. $\tilde{z}/h$ goes from 0 (bottom) to 1 (top).

R_α/h	2	4	10	50	100
			u [10^{-6} m] ($\tilde{z}/h = 0.50$)		
	−21.631	−0.9809	74.853	587.36	1231.1
			w [10^{-5} m] ($\tilde{z}/h = 1.00$)		
	9.7074	15.745	37.713	190.79	383.79
			ψ [A] ($\tilde{z}/h = 0.75$)		
	−98.599	−58.055	−20.601	2.0701	4.9271
			θ [10^{-1} K] ($\tilde{z}/h = 0.25$)		
	2.5176	3.0991	3.2941	3.3317	3.3329
			$\mathcal{B}_z$ [10^{-3} T] ($\tilde{z}/h = 0.75$)		
	12.055	10.996	10.032	6.4691	2.0633
			q_z [10^{-1} W/m^2] ($\tilde{z}/h = 0.50$)		
	−4.1285	−8.5575	−21.684	−108.74	−217.49
			$\sigma_{\alpha\alpha}$ [10^{-3} Pa] ($\tilde{z}/h = 1.00$)		
	−7.0788	4.6343	12.507	17.171	18.284
			σ_{zz} [Pa] ($\tilde{z}/h = 0.25$)		
	3559.7	−518.20	−92.833	0.7001	−10.047

The influence of the shell curvature is evident, as several variables exhibit non-monotonic variations with increasing R_α/h. Moreover, the two loading boundary configurations produce significantly different responses for the transverse displacement w and the magnetic potential ψ, particularly for slender cylindrical panels. These differences arise from the combined effects of structural curvature, the progressive reduction in stiffness as the panel becomes thinner, and the different magnetic boundary conditions prescribed in the LB1 and LB2 configurations.

Table 15. NC3, simply supported sandwich *Adaptive Wood/Soft Adaptive Wood/Adaptive Wood* cylindrical shell panel considering LB2 load boundary conditions. Results are obtained via the 3D-u-θ-ψ model. $\tilde{z}/h$ goes from 0 (bottom) to 1 (top).

R_α/h	2	4	10	50	100
			u [10^{-4} m] ($\tilde{z}/h = 0.50$)		
	−0.2537	−0.0512	−3.1629	−603.76	−4898.2
			w [10^{-4} m] ($\tilde{z}/h = 0.25$)		
	1.1935	2.0632	−6.7576	−1805.0	−14,684
			ψ [10^4 A] ($\tilde{z}/h = 1.00$)		
	1.8794	−2.0373	−3.4472	−15.611	−31.122
			θ [10^{-1} K] ($\tilde{z}/h = 0.25$)		
	2.5176	3.0991	3.2941	3.3317	3.3329
			$\mathcal{B}_z$ [10^{-1} T] ($\tilde{z}/h = 0.50$)		
	2.6225	4.2517	5.0080	5.0171	4.9676
			q_z [10^{-1} W/m^2] ($\tilde{z}/h = 0.75$)		
	−5.1922	−9.1893	−21.956	−108.79	−217.52

Table 15. *Cont.*

R_α/h	2	4	10	50	100
			$\sigma_{\beta\beta}$ [10^5 Pa] ($\tilde{z}/h = 1.00$)		
	-6.1588	-6.9573	-78.808	-2516.5	$-10{,}301$
			σ_{zz} [10^5 Pa] ($\tilde{z}/h = 0.75$)		
	0.5017	0.3756	1.2422	7.1111	14.417

Figures 6 and 7 present the through-the-thickness distributions of the selected variables for representative thickness ratios. In both loading configurations, the zigzag behaviour is clearly identified through the slope changes occurring at each material interface, while the continuity of all variables confirms the correct enforcement of the interlaminar continuity conditions. For this case, the w graphical trends for the two load boundary condition demonstrate a different sign in the flexural behaviour. The combination of load boundary condition and thickness ratio gives a central flexural deformation for the thinner case while gives a external flexural deformation for the thicker case. For what concerns the magnetic potential trend in the LB1 load boundary condition, the peak in the central core of the multilayered structure is due to the single curvature of the geometry. This geometrical anisotropy gives a full coupling in terms of deformation and magnetostrictive properties that creates this behaviour along the thickness direction. The transverse heat flux behaviour is similar to the discussed NC2.

The prescribed loading boundary conditions are correctly recovered at the outer surfaces. In Figure 6, the imposed values are satisfied by the over-temperature θ and the magnetic potential ψ, whereas Figure 7 shows the correct fulfillment of the boundary conditions for θ and the transverse magnetic induction $\mathcal{B}_z$. As no external mechanical pressure is applied, the transverse normal stress σ_{zz} vanishes at both outer surfaces. Overall, the proposed benchmark confirms the capability of the present formulation to accurately reproduce the thermo-magneto-elastic coupling together with the curvature effect, the material layer effect, the thickness effect, the zigzag behaviour, and the interlaminar continuity conditions.

In the fourth new case (NC4), a sandwich spherical shell is investigated. The corresponding geometrical parameters and half-wave numbers are reported in the fourth column of Table 9. Tables 16 and 17 collect representative results for the two loading boundary configurations by considering the in-plane and transverse displacements, magnetic potential ψ, over-temperature θ, transverse magnetic induction $\mathcal{B}_z$, transverse heat flux q_z, in-plane stress components, and transverse normal stress σ_{zz} at selected $\tilde{z}/h$ locations and for different thickness ratios.

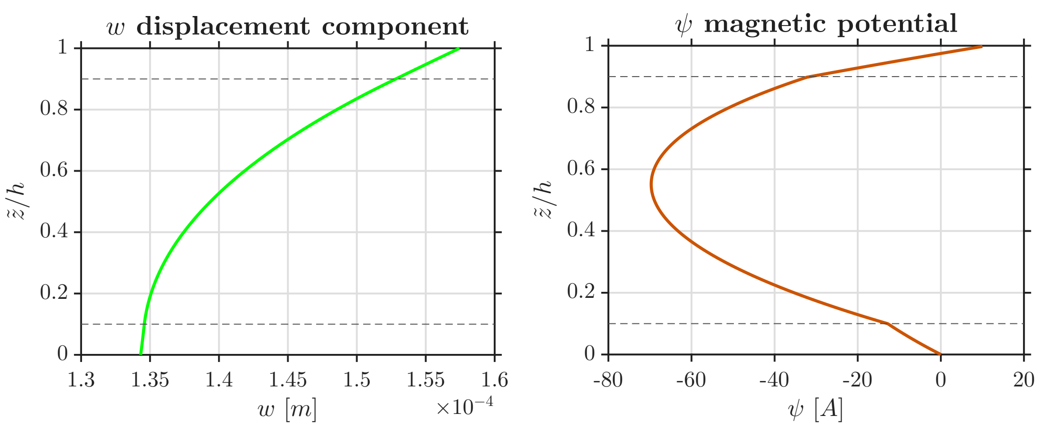

Figure 6. *Cont.*

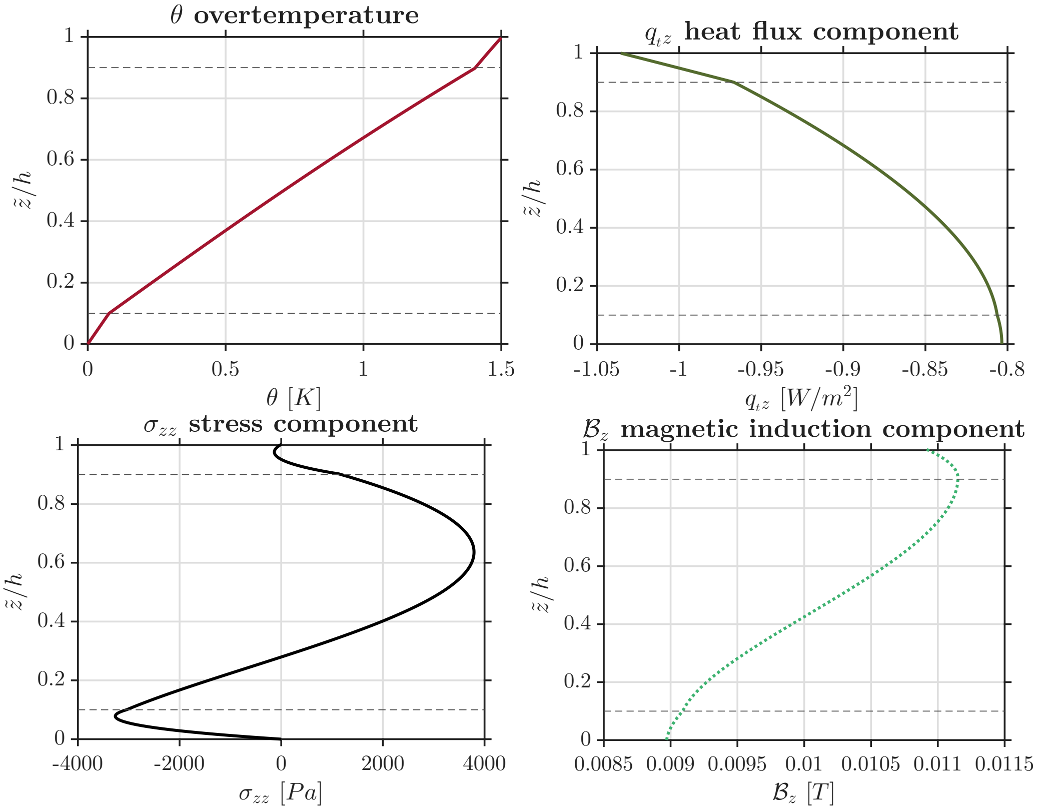

Figure 6. NC3: simply-supported sandwich *Adaptive Wood/Soft Adaptive Wood/Adaptive Wood* cylindrical shell considering LB1 Load Boundary conditions ($\psi_t = 10\,\mathrm{V}$, $\psi_b = 0\,\mathrm{V}$ and $\theta_t = 1.5\,\mathrm{K}$, $\theta_b = 0\,\mathrm{K}$). Thickness ratio is $R_\alpha/h = 4$. Results are obtained via the 3D-u-θ-ψ model.

Similarly to the cylindrical panel discussed in NC3, the magnetic variables are strongly influenced by the prescribed loading boundary conditions. The magnetic potential ψ and the transverse magnetic induction $\mathcal{B}_z$ exhibit different behaviours as the structure changes from thick to thin spherical shells because the magnetic field distribution varies according to the adopted magnetic boundary conditions. In particular, under the LB1 configuration, the magnetic potential changes sign from negative values for thick shells to positive values for thin shells, whereas it remains negative for all thickness ratios under the LB2 configuration. Conversely, the transverse magnetic induction $\mathcal{B}_z$ remains positive for both loading configurations. The in-plane displacement v, transverse displacement w, over-temperature θ, and transverse heat flux q_z exhibit the same overall trend, with increasing values as the shell becomes thinner owing to the progressive reduction in the structural stiffness.

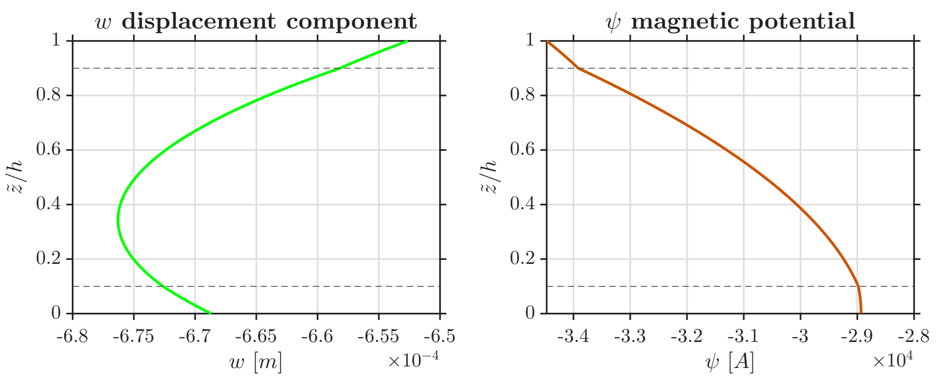

Figure 7. *Cont.*

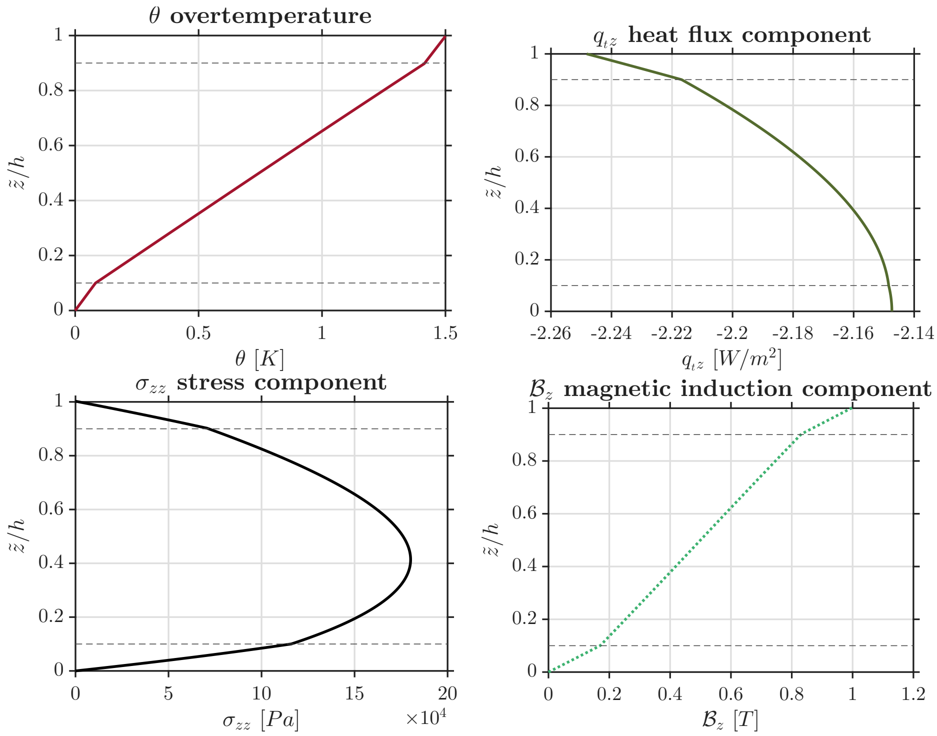

Figure 7. NC3: simply-supported sandwich *Adaptive Wood/Soft Adaptive Wood/Adaptive Wood* cylindrical shell considering LB2 Load Boundary conditions ($\mathcal{B}_{z_t} = 1\,\text{T}$, $\mathcal{B}_{z_b} = 0\,\text{T}$ and $\theta_t = 1.5\,\text{K}$, $\theta_b = 0\,\text{K}$). Thickness ratio is $R_\alpha/h = 10$. Results are obtained via the 3D-u-θ-ψ model.

Figures 8 and 9 present the through-the-thickness distributions of w, ψ, θ, q_z, σ_{zz}, and $\mathcal{B}_z$ for representative thickness ratios under the LB1 and LB2 loading configurations, respectively. In both cases, the zigzag behaviour is clearly identified through the slope changes occurring at the material interfaces, while the continuity of all variables confirms the correct enforcement of the interlaminar continuity conditions. In Figures 8 and 9, the w transverse displacement component in the LB1 configuration is monotonous as the NC2 and NC3 cases while in for the LB2 configuration is non-monotonous due to the magnetostrictive-flexural coupling. Similar magnetic potential trend visible for the NC3 case is here proposed for the two different load boundary conditions. The same considerations done in the NC2 and NC3 case are valid.

The prescribed loading boundary conditions are correctly recovered at the outer surfaces for both loading configurations. Since no external mechanical pressure is applied, the transverse normal stress σ_{zz} vanishes at the top and bottom surfaces of the spherical shell. Overall, the proposed benchmark confirms the capability of the present formulation to accurately reproduce the thermo-magneto-elastic coupling together with the curvature effect, the material layer effect, the thickness effect, the zigzag behaviour, and the interlaminar continuity conditions.

Table 16. NC4, simply supported sandwich *Adaptive Wood/Soft Adaptive Wood/Adaptive Wood* spherical shell panel considering LB1 load boundary conditions. Results are obtained via the 3D-u-θ-ψ model. $\tilde{z}/h$ goes from 0 (bottom) to 1 (top).

R_α/h	2	4	10	50	100
			$v\,[10^{-6}\,\text{m}]$ $(\tilde{z}/h = 0.50)$		
	-5.2934	-3.3591	3.8933	2.3170	1.2555
			$w\,[10^{-5}\,\text{m}]$ $(\tilde{z}/h = 1.00)$		
	7.5816	9.5657	12.718	11.693	11.137

Table 16. *Cont.*

R_α/h	2	4	10	50	100
			ψ [A] ($\tilde{z}/h = 0.75$)		
	-75.188	-52.456	-19.939	2.4566	5.1417
			θ [10^{-1} K] ($\tilde{z}/h = 0.25$)		
	1.9574	2.8877	3.2555	3.3302	3.3325
			$\mathcal{B}_z$ [10^{-3} T] ($\tilde{z}/h = 0.75$)		
	13.077	12.018	10.688	7.0426	2.6077
			q_z [10^{-1} W/m^2] ($\tilde{z}/h = 0.50$)		
	-3.9036	-8.4163	-21.618	-108.72	-217.49
			$\sigma_{\alpha\beta}$ [10^4 Pa] ($\tilde{z}/h = 1.00$)		
	-122.91	-106.19	-48.693	-4.0869	-1.4281
			σ_{zz} [10^3 Pa] ($\tilde{z}/h = 0.25$)		
	88.194	43.405	42.758	14.193	7.3724

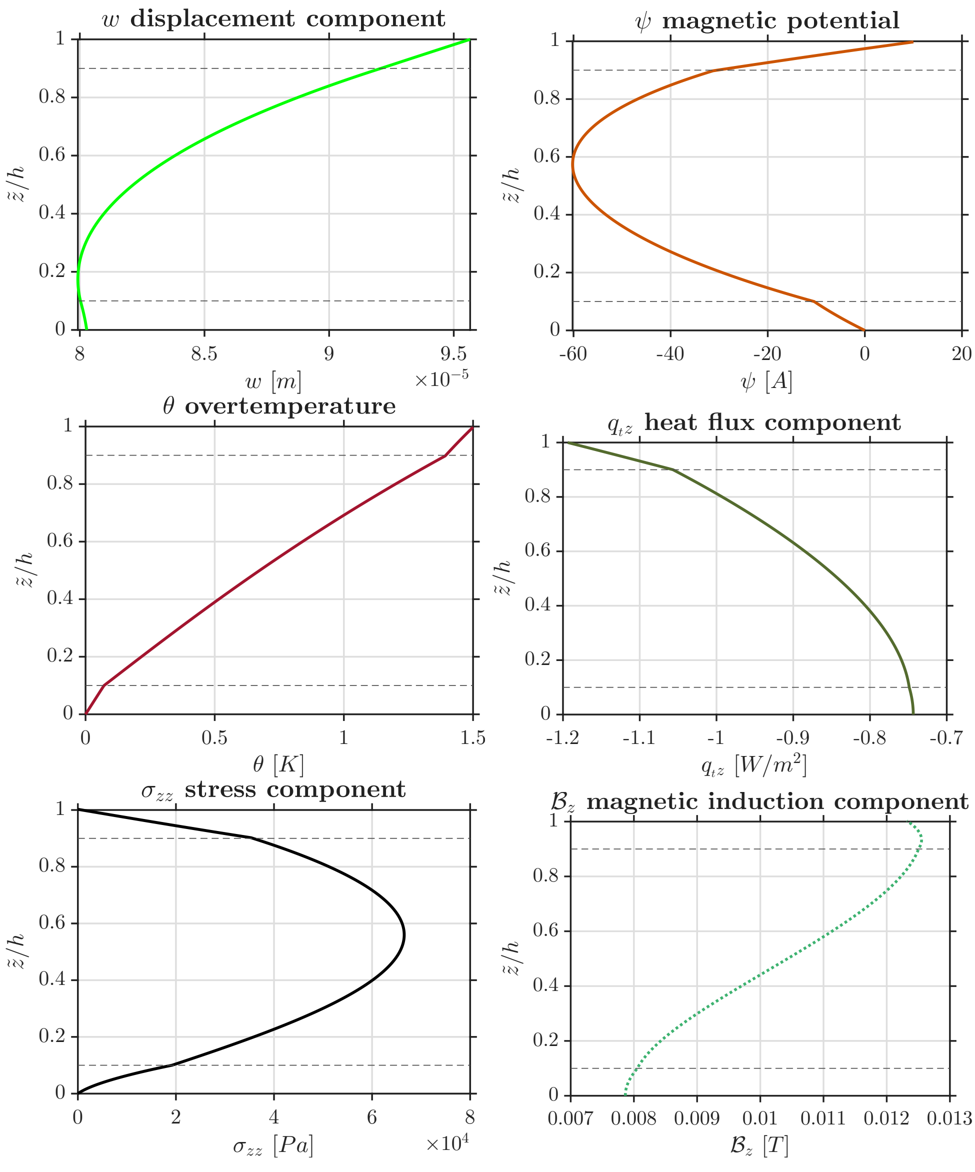

Figure 8. NC4: simply-supported sandwich *Adaptive Wood/Soft Adaptive Wood/Adaptive Wood* spherical shell considering LB1 Load Boundary conditions ($\psi_t = 10$ V, $\psi_b = 0$ V and $\theta_t = 1.5$ K, $\theta_b = 0$ K). Thickness ratio is $R_\alpha/h = 4$. Results are obtained via the 3D-u-θ-ψ model.

Table 17. NC4, simply supported sandwich *Adaptive Wood/Soft Adaptive Wood/Adaptive Wood* spherical shell panel considering LB2 load boundary conditions. Results are obtained via the 3D-u-θ-ψ model. $\tilde{z}/h$ goes from 0 (bottom) to 1 (top).

R_α/h	2	4	10	50	100
			u [10^{-6} m] ($\tilde{z}/h = 0.50$)		
	-8.2575	-5.0205	-8.0864	-121.46	-252.77
			w [10^{-5} m] ($\tilde{z}/h = 0.25$)		
	7.0247	12.430	13.430	22.094	61.911
			ψ [10^{4} A] ($\tilde{z}/h = 1.00$)		
	-1.2547	-1.3101	-1.8844	-7.8247	-15.547
			θ [10^{-1} K] ($\tilde{z}/h = 0.25$)		
	1.9574	2.8877	3.2555	3.3302	3.3325
			$\mathcal{B}_z$ [10^{-1} T] ($\tilde{z}/h = 0.50$)		
	1.5230	3.3447	4.7638	5.0343	5.0226
			q_z [10^{-1} W/m^2] ($\tilde{z}/h = 0.75$)		
	-5.7683	-9.6296	-22.158	-108.83	-217.54
			$\sigma_{\beta\beta}$ [10^{6} Pa] ($\tilde{z}/h = 1.00$)		
	-1.7159	-1.2313	-2.4002	-4.8841	-5.2267
			σ_{zz} [10^{4} Pa] ($\tilde{z}/h = 0.75$)		
	22.480	9.7710	8.2566	3.0020	1.5829

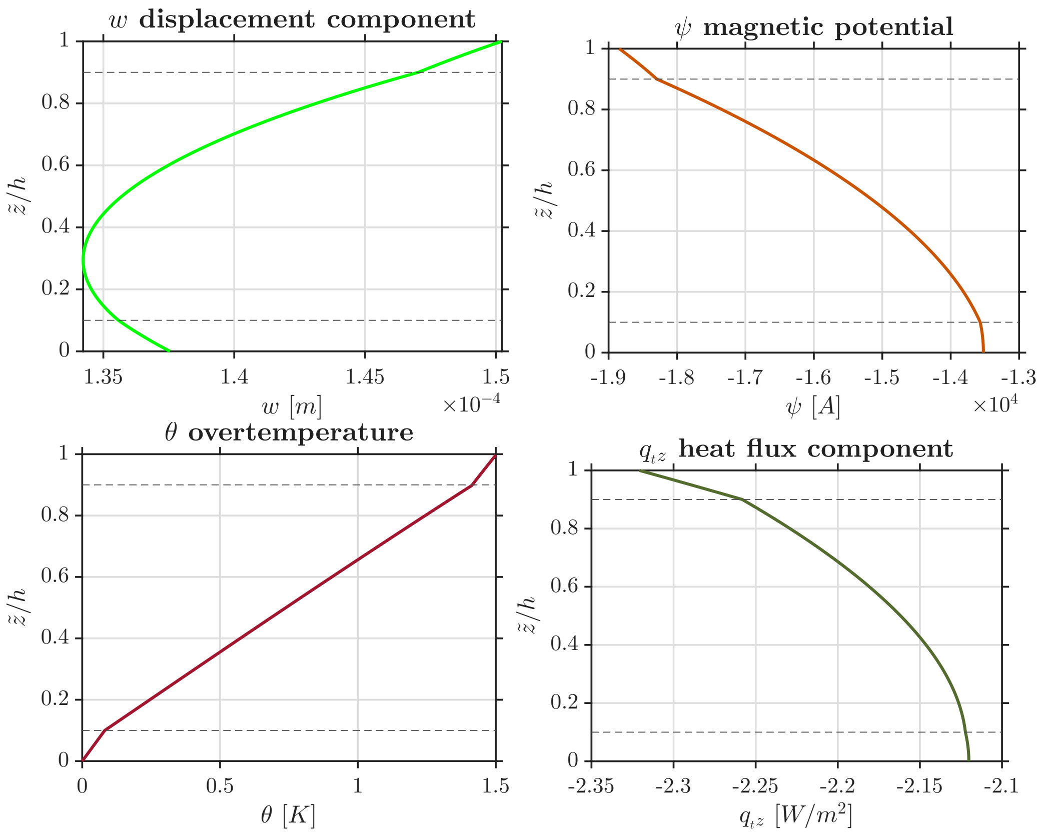

Figure 9. *Cont.*

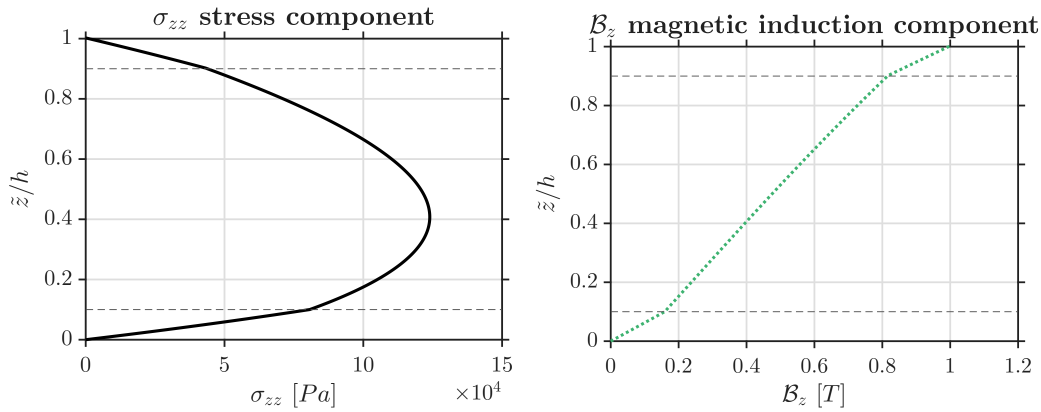

Figure 9. NC4: simply-supported sandwich *Adaptive Wood/Soft Adaptive Wood/Adaptive Wood* spherical shell considering LB2 Load Boundary conditions ($\mathcal{B}_{z_t} = 1\,\mathrm{T}$, $\mathcal{B}_{z_b} = 0\,\mathrm{T}$ and $\theta_t = 1.5\,\mathrm{K}$, $\theta_b = 0\,\mathrm{K}$). Thickness ratio is $R_\alpha/h = 10$. Results are obtained via the 3D-u-θ-ψ model.

4. Conclusions

The present study has introduced a three-dimensional layer-wise coupled thermo-magneto-elastic shell model for the static analysis of multilayered flat and curved smart structures. The governing formulation consists of the three-dimensional elastic equilibrium equations, the magnetic induction divergence equation, and the Fourier heat conduction equation, all fully coupled within a unified multifield framework. The analytical solution for orthotropic simply-supported structures combines Navier harmonic expansions in the in-plane directions with the exponential matrix method along the thickness coordinate. By adopting a mixed orthogonal curvilinear reference system, the proposed formulation provides a unified framework for the analysis of simply supported plates, cylinders, cylindrical panels, and spherical shells through the appropriate definition of the curvature radii. The layer-wise strategy is implemented by enforcing interlaminar continuity conditions on displacements, magnetic potential, over-temperature, transverse shear and normal stresses, transverse magnetic induction, and transverse heat flux by considering perfect interfaces. Different thermal, magnetic, and mechanical loading configurations can be prescribed at the outer surfaces through over-temperature, magnetic potential, and transverse magnetic induction boundary conditions.

The numerical investigation has been divided into two complementary stages. First, the proposed formulation has been validated through comparisons with thermo-magneto-elastic solutions available in the literature. The obtained results demonstrate the capability of the model to accurately reproduce thermo-magneto-elastic coupling, curvature effects, and the influence of both the material sequence and the structural thickness. The validation campaign has been carried out by employing an exponential matrix order equal to $N = 3$ and $M = 300$ mathematical layers, whose adequacy has been confirmed through dedicated convergence analyses. Subsequently, four new benchmark problems involving simply supported sandwich plates, cylinders, cylindrical panels, and spherical shells have been presented. Thick and thin configurations have been investigated under two different loading boundary configurations. The structural response has been evaluated in terms of displacements, magnetic potential, over-temperature, magnetic induction, heat flux, and stress components by means of both tabulated values at selected through-the-thickness locations and graphical distributions along the thickness direction.

The proposed benchmark results clearly demonstrate the capability of the formulation to reproduce all the main physical features characterizing thermo-magneto-elastic multilayered structures. In particular, thermo-magneto-elastic coupling, curvature effects, zigzag behaviour, material layer effects, thickness effects, and interlaminar continuity conditions are accurately captured for both flat and curved geometries. Furthermore, the distributions of the elastic, thermal, and magnetic fields are shown to be strongly affected by the prescribed loading boundary conditions, emphasizing the importance of fully coupled three-dimensional analyses for the design and optimization of smart aerospace structures.

The benchmark solutions generated in this work provide a reliable reference database for researchers developing advanced multifield formulations for smart multilayered structures. Owing to its fully three-dimensional analytical nature, the proposed model can also be employed as a rigorous validation tool for future two-dimensional and three-dimensional analytical or numerical formulations involving coupled thermo-magneto-elastic phenomena.

Author Contributions: Conceptualization, S.B. and D.C.; methodology, S.B.; software, D.C. and S.B.; validation, D.C.; formal analysis, S.B. and D.C.; investigation, D.C.; resources, S.B. and D.C.; data curation, D.C.; writing—original draft preparation, D.C.; writing—review and editing, S.B.; visualization, S.B.; supervision, S.B.; project administration, S.B.; funding acquisition, S.B. All authors have read and agreed to the published version of the manuscript.

Funding: This research received no external funding.

Institutional Review Board Statement: Not applicable.

Informed Consent Statement: Not applicable.

Data Availability Statement: The original contributions presented in this study are included in the article. Further inquiries can be directed to the corresponding author.

Conflicts of Interest: The authors declare no conflicts of interest.

References

1. Liu, P.; Yao, Z.; Zhou, J.; Yang, Z.; Kong, L.-B. Small magnetic Co-doped NiZn ferrite/graphene nanocomposites and their dual-region microwave absorption performance. *J. Mater. Chem. C* **2016**, *4*, 9738–9749. [CrossRef]
2. Habashne, M.; Cucuzza, R.; Domaneschi, M.; Fathnejat, H.; Movahedi, R.M. Thermo-mechanical reliability-based topology optimization for imperfect elasto-plastic materials. *Int. J. Mech. Mater. Des.* **2025**, *21*, 1755–1776. [CrossRef]
3. Guo, Y.; Alam, M. Nonlinear bending and thermal postbuckling of magneto-electro-elastic nonlocal strain-gradient beam including surface effects. *Appl. Math. Model.* **2025**, *142*, 115955. [CrossRef]
4. Ren, S.; Meng, G.; Wang, J.; Zhou, L.; Zhao, H. A stabilized node-based smoothed radial point interpolation method for functionally graded magneto-electro-elastic structures in thermal environment. *Compos. Struct.* **2020**, *234*, 111674. [CrossRef]
5. Ren, S.; Meng, G.; Cheng, F.; Zhou, L. Transient responses of functionally graded magneto-electro-elastic structures with holes in thermal environment using stabilized node-based smoothed radial point interpolation method. *Int. J. Mech. Sci.* **2020**, *185*, 105870. [CrossRef]
6. Ren, Y.-M.; Qing, H. Size-dependent buckling and vibration of functionally graded magneto-electro-thermo-elastic Timoshenko nanobeams using general stress-driven two-phase local/nonlocal integral model. *Thin-Walled Struct.* **2025**, *215*, 113480. [CrossRef]
7. Vinyas, M.; Kattimani, S.C. Static studies of stepped functionally graded magneto-electro-elastic beam subjected to different thermal loads. *Compos. Struct.* **2017**, *163*, 216–237. [CrossRef]
8. Zhang, X.L.; Xu, Q.; Zhao, X.; Li, Y.H.; Yang, J. Nonlinear analyses of magneto-electro-elastic laminated beams in thermal environments. *Compos. Struct.* **2020**, *234*, 111524. [CrossRef]
9. Zhang, X.L.; Chen, X.C.; Li, M.; Li, Y.H.; Xu, J. Thermal post-buckling analyses of magneto-electro-elastic laminated beams via generalized differential quadrature method. *Aerosp. Sci. Technol.* **2021**, *119*, 107179. [CrossRef]
10. Anh, V.T.T.; Dat, N.D.; Nguyen, P.D.; Duc, N.D. A nonlocal higher-order shear deformation approach for nonlinear static analysis of magneto-electro-elastic sandwich micro/nano-plates with FG-CNT core in hygrothermal environment. *Aerosp. Sci. Technol.* **2024**, *147*, 109609. [CrossRef]
11. Esen, I.; Özmen, R. Thermal vibration and buckling of magneto-electro-elastic functionally graded porous nanoplates using nonlocal strain gradient elasticity. *Compos. Struct.* **2022**, *296*, 115878.
12. Li, X.Y.; Dong, Y.H.; Liu, C.; Liu, Y.; Wang, C.J.; Shi, T.F. Axisymmetric thermo-magneto-electro-elastic field in a heterogeneous circular plate subjected to a uniform thermal load. *Int. J. Mech. Sci.* **2014**, *88*, 71–81. [CrossRef]

13. Li, M.; Zhou, L.; Liu, C. The multi-physical cell-based smoothed finite element method for analysing transient behaviour of functionally graded magneto-electro-elastic thin-walled structures under thermal environment. *Thin-Walled Struct.* **2020**, *155*, 106876. [CrossRef]
14. Mahesh, V. Artificial neural network (ANN) based investigation on the static behaviour of piezo-magneto-thermo-elastic nanocomposite sandwich plate with CNT agglomeration and porosity. *Int. J. Non-Linear Mech.* **2023**, *153*, 104406.
15. Mahesh, V.; Mahesh, V.; Ponnusami, S.A. FEM-ANN approach to predict nonlinear pyro-coupled deflection of sandwich plates with agglomerated porous nanocomposite core and piezo-magneto-elastic facings in thermal environment. *Mech. Adv. Mater. Struct.* **2024**, *31*, 4551–4574.
16. Mohammadimehr, M.; Emdadi, M.; Afshari, H.; Navi, B.R. Bending, buckling and vibration analyses of MSGT microcomposite circular-annular sandwich plate under hydro-thermo-magneto-mechanical loadings using DQM. *Int. J. Smart Nano Mater.* **2018**, *9*, 233–260. [CrossRef]
17. Mukahal, F.H.H.A.; Sobhy, M.; Al-Ali, A.H.K. Magneto-hygrothermal deformation of FG nanocomposite annular sandwich nanoplates with porous core using the DQM. *Crystals* **2025**, *15*, 2–32.
18. Talleb, H.; Ren, Z. A new nonlinear multiscale magnetostrictive approach for FEM modelling of magnetoelectric composites under magneto-thermo-elastic loading. *Compos. Struct.* **2023**, *303*, 116260.
19. Vinyas, M.; Kattimani, S.C. Static analysis of stepped functionally graded magneto-electro-elastic plates in thermal environment: A finite element study. *Compos. Struct.* **2017**, *178*, 63–86. [CrossRef]
20. Vinyas, M.; Kattimani, S.C. Hygrothermal analysis of magneto-electro-elastic plate using 3D finite element analysis. *Compos. Struct.* **2017**, *180*, 617–637.
21. Vu, V.-T.; Tran, H.-Q. Thermo-electro-magneto-mechanical vibration analysis of sandwich plates with graphene oxide powder reinforced composite core and magneto-electro-elastic face sheets resting on Kerr foundation. *Int. J. Mech. Mater. Des.* **2025**, *21*, 1609–1641. [CrossRef]
22. Wang, X.; Lee, J.S.; Zheng, X. Magneto-thermo-elastic instability of ferromagnetic plates in thermal and magnetic fields. *Int. J. Solids Struct.* **2003**, *40*, 6125–6142. [CrossRef]
23. Wu, C.-P.; Hsu, C.-D. A unified size-dependent theory for analyzing the free vibration behavior of an FG microplate under fully simply supported conditions and magneto-electro-thermo-mechanical loads considering couple stress and thickness stretching effects. *J. Compos. Sci.* **2025**, *9*, 201. [CrossRef]
24. Xing, Y.; Liu, B. A differential quadrature analysis of dynamic and quasi-static magneto-thermo-elastic stresses in a conducting rectangular plate subjected to an arbitrary variation of magnetic field. *Int. J. Eng. Sci.* **2010**, *48*, 1944–1960. [CrossRef]
25. Zhou, L.; Yang, H.; Ma, L.; Zhang, S.; Li, X.; Ren, S.; Li, M. On the static analysis of inhomogeneous magneto-electro-elastic plates in thermal environment via element-free Galerkin method. *Eng. Anal. Bound. Elem.* **2022**, *134*, 539–552. [CrossRef]
26. Saadatfar, M.; Babazadeh, M.A.; Babaelahi, M. Coupled thermo-mechanical analysis of creep in a rotating FGMEE annular plate under complex thermal loading considering solar radiation, convection, and internal heat source. *Forces Mech.* **2024**, *16*, 100277. [CrossRef]
27. Zenkour, A.M. On the magneto-thermo-elastic responses of FG annular sandwich disks. *Int. J. Eng. Sci.* **2014**, *75*, 54–66. [CrossRef]
28. Brischetto, S.; Cesare, D.; Mondino, T. 3D exact magneto-electro-elastic static analysis of multilayered plates. *CMES Comput. Model. Eng. Sci.* **2025**, *144*, 643–668. [CrossRef]
29. Brischetto, S.; Cesare, D.; Mondino, T. Magneto-electro-elastic 3D coupling in free vibrations of layered plates. *CMC Comput. Mater. Contin.* **2025**, *85*, 4491–4518. [CrossRef]
30. Pham, Q.-H.; Malekzadeh, P.; Tran, V.K.; Nguyen-Thoi, T. Free vibration analysis of functionally graded porous curved nanobeams on elastic foundation in hygro-thermo-magnetic environment. *Front. Struct. Civ. Eng.* **2023**, *17*, 584–605. [CrossRef]
31. Barati, A.R.; Shariyat, M. Novel exact layerwise analytical solution for anisotropic multi-layer magneto-piezo-elastic hollow spheres under asymmetric magneto-electro-hygro-thermo-mechanical loads. *Compos. Struct.* **2022**, *302*, 116227. [CrossRef]
32. Barati, A.R.; Shariyat, M. Exact closed-form solutions for behavior investigation of heterogeneous piezo-magneto-elastic discs under magneto-electro-hygro-thermo-mechanical loads. *Eur. J. Mech. A Solids* **2023**, *101*, 105066. [CrossRef]
33. Bian, Y.H.; Tian, Z.G. Nonlinear theory of thermomagnetoelasticity of spherical segment shells with Joule's heat taken into account. *Int. Appl. Mech.* **2023**, *59*, 370–380. [CrossRef]
34. Dai, H.L.; Wang, X. Magneto–thermo–electro–elastic transient response in a piezoelectric hollow cylinder subjected to complex loadings. *Int. J. Solids Struct.* **2006**, *43*, 5628–5646. [CrossRef]
35. Gui, Y.; Wu, R. Buckling analysis of embedded thermo-magneto-electro-elastic nano cylindrical shell subjected to axial load with nonlocal strain gradient theory. *Mech. Res. Commun.* **2023**, *128*, 104043. [CrossRef]
36. Higuchi, M.; Kawamura, R.; Tanigawa, Y. Dynamic and quasi-static behaviors of magneto-thermo-elastic stresses in a conducting hollow circular cylinder subjected to an arbitrary variation of magnetic field. *Int. J. Mech. Sci.* **2008**, *50*, 365–379. [CrossRef]

37. Higuchi, M.; Kawamura, R.; Tanigawa, Y. Magneto-thermo-elastic stresses induced by a transient magnetic field in a conducting solid circular cylinder. *Int. J. Solids Struct.* **2007**, *44*, 5316–5335. [CrossRef]
38. Hu, Y.-D.; Yang, T.; Cao, T. Magneto-thermo-elastic coupling vibration and bifurcation characteristics of functionally graded rotating cylindrical shell. *Commun. Nonlinear Sci. Numer. Simul.* **2024**, *128*, 107611. [CrossRef]
39. Hu, Y.-D.; Zhou, Q.; Yang, T. Magneto-thermo-elastic coupled free vibration and nonlinear frequency analytical solutions of FGM cylindrical shell. *Thin-Walled Struct.* **2024**, *195*, 111406. [CrossRef]
40. Kong, T.; Li, D.X.; Wang, X. Thermo-magneto-dynamic stresses and perturbation of magnetic field vector in a non-homogeneous hollow cylinder. *Appl. Math. Model.* **2009**, *33*, 2939–2950. [CrossRef]
41. Loghman, A.; Parsa, H. Exact solution for magneto-thermo-elastic behaviour of double-walled cylinder made of an inner FGM and an outer homogeneous layer. *Int. J. Mech. Sci.* **2014**, *88*, 93–99. [CrossRef]
42. Ni, Y.; Sun, J.; Zhang, J.; Tong, Z.; Zhou, Z.; Xu, X. Accurate buckling analysis of magneto-electro-elastic cylindrical shells subject to hygro-thermal environments. *Appl. Math. Model.* **2023**, *118*, 798–817. [CrossRef]
43. Oveissi, S.; Ghassemi, A.; Salehi, M.; Eftekhari, S.A.; Ziaei-Rad, S. Hydro–hygro–thermo–magneto–electro elastic wave propagation of axially moving nano-cylindrical shells conveying various magnetic-nano-fluids resting on the electromagnetic-visco-Pasternak medium. *Thin-Walled Struct.* **2022**, *173*, 108926. [CrossRef]
44. Selvamani, R.; Ebrahimi, F.; Yaylaci, M.; Öztürk, S.; Yaylacı, E.U. Nonlinear poro-thermo-forced vibration in curved sandwich magneto-electro elastic shells under hygrothermal environment. *Acta Mech.* **2024**, *235*, 5489–5528. [CrossRef]
45. Tong, Z.H.; Lo, S.H.; Jiang, C.P.; Cheung, Y.K. An exact solution for the three-phase thermo-electro-magneto-elastic cylinder model and its application to piezoelectric–magnetic fiber composites. *Int. J. Solids Struct.* **2008**, *45*, 5205–5219. [CrossRef]
46. Tornabene, F.; Viscoti, M.; Dimitri, R. Hygro-thermal coupling effect on the magneto-mechanical response of curved laminated structures. *Compos. Struct.* **2025**, *370*, 119329. [CrossRef]
47. Tornabene, F.; Viscoti, M.; Dimitri, R.; Rabczuk, T. Thermo-magneto-mechanical analysis of curved laminated structures with arbitrary variation of the material properties and novel recovery procedure. *Eng. Anal. Bound. Elem.* **2025**, *176*, 106232. [CrossRef]
48. Tornabene, F.; Viscoti, M.; Dimitri, R. Equivalent layer-wise theory for the hygro-thermo-magneto-electro-elastic analysis of laminated curved shells. *Thin-Walled Struct.* **2024**, *198*, 111751. [CrossRef]
49. Zhang, L.; Liu, X. Buckling and vibration analysis of functionally graded magneto-electro-thermo-elastic circular cylindrical shells. *Appl. Math. Model.* **2013**, *37*, 2279–2292. [CrossRef]
50. Brischetto, S.; Cesare, D. A 3D shell model for static and free vibration analysis of multilayered magneto-elastic structures. *Thin-Walled Struct.* **2025**, *206*, 112620. [CrossRef]
51. Brischetto, S.; Torre, R.; Cesare, D. Three dimensional coupling between elastic and thermal fields in the static analysis of multilayered composite shells. *CMES Comput. Model. Eng. Sci.* **2023**, *136*, 2551–2594. [CrossRef]
52. Brischetto, S.; Cesare, D.; Mondino, T. Three-dimensional static analysis of magneto-electro-elastic composite shells. *Compos. Struct.* **2025**, *374*, 119725. [CrossRef]
53. Brischetto, S.; Cesare, D.; Mondino, T. An exact 3D shell model for free vibration analysis of magneto-electro-elastic composite structures. *J. Compos. Sci.* **2025**, *9*, 399. [CrossRef]
54. Ponnusamy, P.; Selvamani, R. Wave propagation in a transversely isotropic magneto thermo elastic cylindrical panel. *Eur. J. Mech. A/Solids* **2013**, *39*, 76–85. [CrossRef]
55. Hildebrand, F.B.; Reissner, E.; Thomas, G.B. *Notes on the Foundations of the Theory of Small Displacements of Orthotropic Shells*; Technical Note No. 1833; NACA—National Advisory Committee for Aeronautics: Washington, DC, USA, 1949. [CrossRef]
56. Povstenko, Y. *Fractional Thermoelasticity*; Springer International Publishing: Cham, Switzerland, 2015. [CrossRef]
57. Brischetto, S.; Torre, R. Convergence investigation for the exponential matrix and mathematical layers in the static analysis of multilayered composite structures. *J. Compos. Sci.* **2017**, *1*, 19.
58. Tornabene, F. *Hygro-Thermo-Magneto-Electro-Elastic Theory of Anisotropic Doubly-Curved Shells*; Società Editrice Esculapio: Bologna, Italy, 2023.
59. Heyliger, P.R.; Pan, E. Static Fields in Magnetoelectroelastic Laminates. *AIAA J.* **2004**, *42*, 1435–1443. [CrossRef]
60. Kulikov, G.M.; Plotnikova, S.V. Exact 3D thermoelectroelastic analysis of piezoelectric plates through a sampling surfaces method. *Mech. Adv. Mater. Struct.* **2015**, *22*, 33–43.
61. Pan, E. Three-dimensional Green's functions in anisotropic magneto-electro-elastic bimaterials. *Z. Angew. Math. Phys.* **2002**, *53*, 815–838. [CrossRef]